Journal of Quantitative Spectroscopy & Radiative Transfer 218 (2018) 131–150

Contents lists available at ScienceDirect

Journal of Quantitative Spectroscopy & Radiative Transfer

journal homepage: www.elsevier.com/locate/jqsrt

Optical tweezers and their applications

Paolo Polimeno[a,1], Alessandro Magazzù[b,1], Maria Antonia Iatì[a,*], Francesco Patti[a,c], Rosalba Saija[a,c], Cristian Degli Esposti Boschi[d], Maria Grazia Donato[a], Pietro G. Gucciardi[a], Philip H. Jones[e], Giovanni Volpe[b], Onofrio M. Maragò[a,*]

[a] CNR-IPCF, Istituto per i Processi Chimico-Fisici, Viale F. Stagno d'Alcontres 37, Messina I-98158, Italy
[b] Institutionen för Fysik, Göteborgs Universitet, Origovägen 6 B, Göteborg I-41296, Sweden
[c] Dipartimento di Scienze Matematiche e Informatiche, Scienze Fisiche e Scienze della Terra, Università di Messina, Viale F. Stagno d'Alcontres, 31, Messina I-98166, Italy
[d] CNR-IMM sezione di Bologna, Istituto per la Microelettronica e Microsistemi, Via P. Gobetti 101, Bologna I-40129, Italy
[e] Department of Physics and Astronomy, University College London, Gower Street, London WC1E 6BT, UK

ARTICLE INFO

Article history:
Received 18 June 2018
Revised 13 July 2018
Accepted 16 July 2018
Available online 19 July 2018

Keywords:
Optical trapping
Optical manipulation
T-matrix
Spectroscopic tweezers
Critical Casimir forces
Active matter

ABSTRACT

Optical tweezers, tools based on strongly focused light, enable optical trapping, manipulation, and characterisation of a wide range of microscopic and nanoscopic materials. In the limiting cases of spherical particles either much smaller or much larger than the trapping wavelength, the force in optical tweezers separates into a conservative gradient force, which is proportional to the light intensity gradient and responsible for trapping, and a non-conservative scattering force, which is proportional to the light intensity and is generally detrimental for trapping, but fundamental for optical manipulation and laser cooling. For non-spherical particles or at intermediate (meso)scales, the situation is more complex and this traditional identification of gradient and scattering force is more elusive. Moreover, shape and composition can have dramatic consequences for optically trapped particle dynamics. Here, after an introduction to the theory and practice of optical forces with a focus on the role of shape and composition, we give an overview of some recent applications to biology, nanotechnology, spectroscopy, stochastic thermodynamics, critical Casimir forces, and active matter.

1. Introduction

Mechanical effects of light are known since Kepler's explanation of comets tail [1]. The advent of the laser has brought to novel concepts and applications of optical forces yielding a real scientific revolution [2–4]. *Optical tweezers* [5] (OT), in their simplest configuration, are instruments based on a tightly focused laser beam that is capable to trap and manipulate a wide range of particles in its focal spot [6]. Since their first demonstration in 1986 by Sir Ashkin et al. [5], they have become a key technique for the trapping, manipulation, and characterisation of atoms [7], microscopic [8,9] and nanoscopic particles [10], as well as biomolecules, viruses, bacteria and cells [11–13]. When used as a force transducer, optical tweezers are able to measure forces in the femtonewton range [6,10]. The concept of photonic force microscopy has been also developed by scanning a trapped particle over surfaces in a liquid environment and sensing the force interaction between trapped probe and surface [14,15].

Despite the tremendous progress in optical trapping techniques, the development of an accurate theoretical modeling for optical tweezers has been slower and often based on approximations [6]. In the limiting cases of spherical particles either much smaller (*dipole approximation*) [16] or much larger (*ray optics approximation*) [17] than the trapping wavelength, the force in optical tweezers separates into two different contributions: a conservative *gradient force*, proportional to the light intensity gradient, responsible for trapping, that can be related to an effective potential, and a non-conservative *scattering force*, that has a dissipative nature, cannot be related to an effective potential, is proportional to the light intensity and is generally detrimental for trapping, but fundamental for optical manipulation and laser cooling [6,10]. However, for non-spherical particles or at intermediate (meso) scales, the situation is more complex and this traditional identification of gradient and scattering force is more elusive [18]. Moreover, shape and composition can have dramatic consequences for the dynamics of optically trapped particles [10,19–21].

* Corresponding authors.
E-mail addresses: mariaantonia.iati@cnr.it (M.A. Iatì), onofrio.marago@cnr.it (O.M. Maragò).
[1] These authors contributed equally to this work.

https://doi.org/10.1016/j.jqsrt.2018.07.013
0022-4073/

Here, we first give a review on the theory of optical forces and optical trapping with a focus on modeling optical tweezers with *T-matrix* methods. Then we discuss some of the most common experimental implementation and methods for optical force calibration. Finally, we discuss a selection of recent applications in biology, nanotechnology, spectroscopy, critical Casimir forces, stochastic thermodynamics, and active matter.

2. Optical forces and optical tweezers

Optical trapping of particles is a consequence of the radiation force that stems from the conservation of electromagnetic momentum upon scattering [6,22]. Historically, the theoretical understanding of this physical process has been investigated through the use of suitable approximations that depend on the size of the particle with respect to the light wavelength [4]. While calculations based on a full electromagnetic theory and the integration of the Maxwell stress tensor [6] can be rather complex and computationally intensive, exploiting approximations can be an advantage, e.g., when combining optical force modeling with stochastic simulations [23,24].

For calculating optical forces acting on spherical or quasi-spherical particles, it is customary to identify several regimes which depend on the particle size [6]. For each regime, simplifications and approximations have been made for a better and more quantitative understanding and calculation of optical forces. The *size parameter*, $x = k_{\mathrm{m}}a$, is crucially used to determine the range of validity of these approximations, where $k_{\mathrm{m}} = 2\pi n_{\mathrm{m}}/\lambda_0$ is the light wavenumber in the medium surrounding the particle, a is the particle radius, λ_0 is the laser wavelength in vacuum used for trapping and n_{m} is the refractive index of the surrounding dielectric, non-magnetic, non-absorbing medium. When the particle size is much bigger than the wavelength of the laser beam, that is $x \gg 1$, optical trapping forces can be calculated with the *ray optics approximation* [25]. The accuracy of this approximation increases with the size parameter, whereas electromagnetic scattering theories might become unpractical due to increasing computational complexity. This makes ray optics very useful when dealing with large particles. However, we note that ray optics is approximate by definition as it ignores the information on the phase of the incident electromagnetic wave and all related interference effects [26]. Thus, the lower size limit of validity is often dependent on the computed quantity [27–29]. If the size of the particle is much smaller than λ_0 ($x \ll 1$), we can adopt the *dipole approximation* and consider the particle as a dipole [16,30,31]. This means we are considering the electromagnetic fields homogeneous inside the particle under the condition $|n_{\mathrm{p}}/n_{\mathrm{m}}|x \ll 1$, where n_{p} is the refractive index of the particle. This condition has to be considered with care when dealing with high refractive index dielectric particles (e.g., silicon) or noble metal (e.g., gold, silver) nanoparticles, where the presence of plasmonic resonances dominate the optical response [32]. In the intermediate regime, that is when the particle size is comparable with the light wavelength ($x \simeq 1$) or for highly non-spherical or non-homogeneous particles, we need a complete wave-optical modeling of the particle-light interaction to calculate the trapping forces and different methods can be considered [6].

2.1. Ray optics

In the ray optics regime [17] the optical field is described by considering it as a collection of N light rays and employing the tools of geometrical optics [6]. Each ray carries with it a portion of the incident power, P_{i}, so that the total power is $P_{\mathrm{i}} = N\sum_{\mathrm{m}} P_{\mathrm{i}}^{(m)}$, and a linear momentum per second $n_{\mathrm{m}}P_{\mathrm{i}}^{(m)}/c$. When a ray impinges on a surface with an incident angle θ_{i}, it will be partly reflected and partly transmitted with a transmitted angle θ_{t}, according to the Snell's law [33]. As a consequence of energy conservation, the power is split between the reflected and transmitted part of the ray following Fresnel coefficients [23]. Moreover, at each scattering event, the ray changes its direction and hence its momentum change causes a reaction force on the center of mass of the particle. Most of the power carried by the incident ray is delivered to the transmitted ray that travels inside the particle until it impinges on the opposite surface. Here it will be reflected and transmitted again and a large portion of the power will be transmitted outside the sphere. The process will continue until all light escapes from the sphere.

In general, if more than one ray interacts with a particle, the total force is given by the sum of the forces generated by the reflection and refraction of each ray. For simplicity we consider in the following a highly focused laser beam impinging on a spherical particle. To calculate the optical force of the focused beam, we model it as a set of many rays that converge at a very large angle in the focal spot. Thus, we need to sum up all force contributions, $\mathbf{F}_{\mathrm{ray}}^{(m)}$, associated to the reflection and transmission of each mth ray with power $P_{\mathrm{i}}^{(m)}$ in the direction $\hat{\mathbf{r}}_{\mathrm{i}}^{(m)}$ forming the beam. Thus, the total force acting on the centre of mass of the sphere is $\mathbf{F}_{\mathrm{GO}} = \sum_m \mathbf{F}_{\mathrm{ray}}^{(m)}$, and more explicitly [6,23]:

$$\mathbf{F}_{\mathrm{GO}} = \sum_m \left[\frac{n_{\mathrm{m}}P_{\mathrm{i}}^{(m)}}{c}\hat{\mathbf{r}}_{\mathrm{i}}^{(m)} - \frac{n_{\mathrm{m}}P_{\mathrm{r}}^{(m)}}{c}\hat{\mathbf{r}}_{\mathrm{r},0}^{(m)} - \sum_{j=1}^{+\infty}\frac{n_{\mathrm{p}}P_{\mathrm{t},j}^{(m)}}{c}\hat{\mathbf{r}}_{\mathrm{t},j}^{(m)} \right]. \tag{1}$$

where $\hat{\mathbf{r}}_{\mathrm{r},0}^{(m)}$, $P_{\mathrm{r}}^{(m)}$ and $\hat{\mathbf{r}}_{\mathrm{t},j}^{(m)}$, $P_{\mathrm{t},j}^{(m)}$ are the unit vector and power in the direction of the reflected 0-ray and the transmitted jth ones, respectively. Each optical force, associated with the mth ray, has components only in the incidence plane and can be split in two perpendicular components (note that this is valid only for spheres). The component in the direction of the incoming ray represents the scattering force that pushes the particle away from the center of the trap. The component perpendicular to the incoming ray is the gradient force, that pulls the particle towards the optical axis when $n_{\mathrm{m}} < n_{\mathrm{p}}$. Instead, if $n_{\mathrm{m}} > n_{\mathrm{p}}$ the particle is pushed away from the high intensity focal region and different optical trapping strategies must be used [34]. It is often useful to define the dimensionless quantities (trapping efficiencies) obtained dividing these force components by $n_{\mathrm{m}}P_{\mathrm{i}}^{(m)}/c$, that quantify how efficiently the momentum is transferred from the ray to the particle.

For a single-beam optical tweezers, the focused rays will generate a restoring force proportional to the particle's displacement from an equilibrium point, that is for small displacements optical trapping can be modeled as an harmonic response. Due to the scattering force, the particle is displaced away from the focal point to an equilibrium position $\mathbf{C}_{\mathrm{eq}} = [x_{\mathrm{eq}}, y_{\mathrm{eq}}, z_{\mathrm{eq}}]$. Thus, for small displacements optical trapping forces are approximated as Hookean restoring forces, i.e., $F_x \approx -\kappa_x(x - x_{\mathrm{eq}})$, that can be related to an effective harmonic potential with trap stiffnesses κ_x, κ_y and κ_z.

A ray optics approach can be employed to study more complex particle shapes as long as the characteristic particle dimensions are much larger than the wavelength. For non-spherical particles two main differences occur. First, an optical torque can be generated from the difference between the angular momentum carried by the incoming rays and the outgoing rays with respect to the particle center-of-mass [6]. This shape-dependent optical torque can yield alignment [35] or rotation [36] of the particle. The second difference is the occurrence of a transverse component of the radiation pressure, i.e., a set of parallel rays on a non-spherical particle can produce a force transverse to the incident light propagation direction, yielding an *optical lift effect* [37].

2.2. Dipole approximation

When the particle size parameter is small, $x \ll 1$, optical trapping forces can be calculated exploiting a dipole approximation, i.e., the particle can be approximated as a small induced dipole immersed in an electromagnetic field $\mathbf{E}(\mathbf{r}, t)$, which can be considered homogeneous inside the particle ($x|n_\mathrm{p}/n_\mathrm{m}| \ll 1$) [30]. An induced dipole is thus generated and experiences electrostatic forces arising from its interaction with the inducing electric field. Consequently, an oscillating electromagnetic field, such as that of the laser beam used for an optical tweezers, induces an oscillating dipole, which also experiences forces arising from its interaction with the inducing electromagnetic field. Furthermore, an oscillating dipole radiates an electromagnetic field that can produce a mechanical effect on other induced dipoles leading to, in some cases, *optical binding* [38].

This picture can be extended to a small particle, so that if the external field is not too large, the induced dipole moment, $\mathbf{p}(\mathbf{r}, t)$, can be expressed in terms of a linear complex polarisability, α_p, with respect to the surrounding medium, given by Draine and Goodman [39]:

$$\alpha_\mathrm{p} = \alpha_0 \left(1 - i\frac{k_\mathrm{m}^3 \alpha_0}{6\pi\varepsilon_\mathrm{m}}\right)^{-1} \tag{2}$$

with ε_m dielectric permittivity of the medium and α_0 being the static Clausius–Mossotti polarisability, $\alpha_0 = 3V\varepsilon_\mathrm{m}\left(\varepsilon_\mathrm{p} - \varepsilon_\mathrm{m}\right)/\left(\varepsilon_\mathrm{p} + 2\varepsilon_\mathrm{m}\right)$, where V is the particle volume and ε_p the dielectric permittivity of the particle.

The polarisability in the dipole regime is linked to the cross-sections. In fact, the light-particle interaction, including optical forces, can be described in terms of extinction, σ_ext, scattering, σ_scat, and absorption, $\sigma_\mathrm{abs} = \sigma_\mathrm{ext} - \sigma_\mathrm{scat}$. For a small particle of polarisability α_p, we can write the extinction and scattering cross-sections as [6]:

$$\sigma_\mathrm{ext,d} = \frac{k_\mathrm{m}}{\varepsilon_\mathrm{m}} \Im\{\alpha_\mathrm{p}\}, \qquad \sigma_\mathrm{scat,d} = \frac{k_\mathrm{m}^4}{6\pi\varepsilon_\mathrm{m}^2} |\alpha_\mathrm{p}|^2. \tag{3}$$

Thus, we can consider the time-averaged optical force experienced by a small particle when illuminated by a time-varying electromagnetic field [16,31,40]:

$$\langle \mathbf{F} \rangle_\mathrm{DA} = \frac{1}{2} \Re\left\{ \sum_i \alpha_\mathrm{p} E_i \nabla E_i^* \right\}. \tag{4}$$

where E_i are the electric field components. Starting from this expression, one can explicitly write the optical force in terms of extinction cross-section and particle's polarisability [16,31,40–42]:

$$\langle \mathbf{F} \rangle_\mathrm{DA} = \frac{1}{2}\frac{n_\mathrm{m}}{c\varepsilon_\mathrm{m}} \Re\{\alpha_\mathrm{p}\} \nabla I(\mathbf{r}) + \frac{n_\mathrm{m}}{c}\sigma_\mathrm{ext}\langle \mathbf{S} \rangle - \frac{1}{2} c n_\mathrm{m} \sigma_\mathrm{ext} \nabla \times \langle \mathbf{s} \rangle, \tag{5}$$

where $I(\mathbf{r}) = \frac{1}{2} n_\mathrm{m} c |\mathbf{E}(\mathbf{r})|^2$ is the intensity of the electric field, $\langle \mathbf{S} \rangle = \frac{1}{2}\Re\{\mathbf{E} \times \mathbf{H}^*\}$ is the time-averaged Poynting vector of the incoming wave and $\langle \mathbf{s} \rangle = i\frac{\varepsilon_\mathrm{m}}{2\omega}\mathbf{E} \times \mathbf{E}^*$ is the time-averaged spin angular momentum density [40–42].

The first term in Eq. (5) represents the gradient force and is responsible for particle confinement in optical tweezers. Arising from the potential energy of a dipole immersed in the electric field, it is conservative. Particles with a positive $\Re\{\alpha_\mathrm{p}\}$ will be attracted toward the high intensity region of the optical field. Conversely, when the real part of the polarisability is negative the particles are repelled by the high intensity region. As an example, for an incident paraxial laser beam with a typical Gaussian intensity profile which propagates along the z axis, the trap stiffnesses $\kappa_{\mathrm{G},\rho}$ in the polarisation plane and $\kappa_{\mathrm{G},z}$ along the direction of propagation related to the gradient force are [43]:

$$\kappa_{\mathrm{G},\rho} = 2\frac{\Re\{\alpha_\mathrm{p}\}}{c n_\mathrm{m}} \frac{I_0}{w_0^2}, \qquad \kappa_{\mathrm{G},z} = \frac{\Re\{\alpha_\mathrm{p}\}}{c n_\mathrm{m}} \frac{I_0}{z_0^2}. \tag{6}$$

where I_0 is the maximum intensity at the center of the beam, w_0 is the Gaussian beam waist, and z_0 is the beam Rayleigh range [6].

The second term in Eq. (5) is the scattering force. It is responsible for the radiation pressure and is non-conservative. Furthermore, it is directed along the propagation direction of the laser beam [3]. The last term in Eq. (5) is a spin-dependent force [40,41]. This term is also non-conservative and dependent on the extinction cross-section. It can be generated by polarisation gradients in the electromagnetic field, but usually does not play a major role in optical trapping because it is either zero or very small compared to the other contributions. However, it may play a more significant role when considering optical trapping with optical beams of higher order with inhomogeneous polarisation patterns such as cylindrical vector beams [44–46] or superpositions of circularly polarised Hermite–Gauss beams [47]. Note that the time-averaged Poynting vector can be decomposed into the sum of an orbital and spin momentum density [48] and hence the non-conservative optical forces are related to the orbital component of the field momentum directed as the local wavevector [40,49]. Thus, spin-dependent optical forces occur when the Poynting vector is not directed as the local wavevector and a transverse spin-dependent force component occurs [50,51].

2.3. Electromagnetic theory and modeling

Particles illuminated by a radiation field experience a radiation force $\mathbf{F}_\mathrm{rad}$ and torque $\mathbf{\Gamma}_\mathrm{rad}$, which contribute to determining their dynamical behaviour. Since the interaction between radiation and matter is regulated by conservation laws, it is possible to derive $\mathbf{F}_\mathrm{rad}$ and $\mathbf{\Gamma}_\mathrm{rad}$ using the conservation of linear and angular momentum. So, the time-averaged optical force and torque exerted by a monochromatic light on a particle are [22,52–54]:

$$\mathbf{F}_\mathrm{rad} = \oint_S \hat{\mathbf{n}} \cdot \langle \mathsf{T}_\mathrm{M} \rangle \, \mathrm{d}S \,, \qquad \mathbf{\Gamma}_\mathrm{rad} = -\oint_S (\langle \mathsf{T}_\mathrm{M} \rangle \times \mathbf{r}) \cdot \hat{\mathbf{n}} \, \mathrm{d}S, \tag{7}$$

where the integration is carried out over the surface S surrounding the scattering particle, $\hat{\mathbf{n}}$ is the outward normal unit vector, $\mathbf{r}$ is the vector position, and $\langle \mathsf{T}_\mathrm{M} \rangle$ is the averaged Maxwell stress tensor which describes the mechanical interaction of light with matter [55]. The general expression of the Maxwell stress tensor in a medium in the Minkowski form [6] can be simplified since we consider always harmonic fields, at angular frequency ω in a homogeneous, linear, and non-dispersive medium. In fact, writing the real physical fields, e.g., $\mathcal{E}(\mathbf{r}, t) = \Re\left\{\mathbf{E}(\mathbf{r}) e^{-i\omega t}\right\}$, in terms of the complex amplitudes, e.g., $\mathbf{E} = \mathbf{E}(\mathbf{r})$, the averaged Maxwell stress tensor simplifies as [6,18]:

$$\langle \mathsf{T}_\mathrm{M} \rangle = \frac{\varepsilon_\mathrm{m}}{2} \Re\left\{ \mathbf{E} \otimes \mathbf{E}^* + \frac{c^2}{n_\mathrm{m}^2} \mathbf{B} \otimes \mathbf{B}^* - \frac{1}{2}\left(|\mathbf{E}|^2 + \frac{c^2}{n_\mathrm{m}^2} |\mathbf{B}|^2 \right) \mathsf{I} \right\}, \tag{8}$$

where the fields, $\mathbf{E} = \mathbf{E}_\mathrm{i} + \mathbf{E}_\mathrm{s}$ and $\mathbf{B} = \mathbf{B}_\mathrm{i} + \mathbf{B}_\mathrm{s}$, are the total electric and magnetic fields, superposition of the incident ($\mathbf{E}_\mathrm{i}$, $\mathbf{B}_\mathrm{i}$) and scattered ($\mathbf{E}_\mathrm{s}$, $\mathbf{B}_\mathrm{s}$) fields and I is the dyadic unit.

Several techniques have been proposed for computing electromagnetic scattering by non spherical particles and actually there is no single universal method that provides the best results in all cases. Depending on the specific particle parameters, one particular technique may prove to be the most appropriate in terms of efficiency, accuracy, and applicability [26]. While a comprehensive overview of numerical methods for optical tweezers it is beyond the scope of this work, some cover of the topic can be found elsewhere [56–59]. Here we give a very brief description of some common computational methods that have been applied to the model-

ing of optical trapping of irregular shaped particles, such as discrete dipole approximation [60,61] (DDA), finite-difference time-domain [62,63] (FDTD), and we focus our attention to transition (T-)matrix [64] methods with some notes on the connection with generalised Lorenz-Mie theories [65] (GLMTs).

The DDA is a finite element method originally devised by Purcell and Pennypacker [66] and later improved by Draine and Flatau [67]. In the DDA method, a particle is split into a series of dipoles, each of which interacts with the incident electromagnetic wave and with the electromagnetic waves re-radiated by all the other dipoles [60,61]. DDA methods have been applied successfully to optical tweezers modeling of both single-beam optical trapping of non-spherical particles [68] and holographic multiple trapping of complex shaped structures [69,70]. The FDTD, instead, is based on the numerical integration of the Maxwell equations in the time domain [62,63]. The electric and magnetic fields are sampled at discrete times and positions and, therefore, do not assume a harmonic time-dependence. Applications of FDTD to optical trapping problems have been explored for single-beam [71] and holographic [72] optical tweezers. More recently, finite elements methods have been also used to model optical trapping by near-field and plasmonic structures [73,74]. The DDA and FTDT methods, although more computationally intensive than T-matrix or GLMT, can be readily applied to particles of any shape and composition, and to any light field configuration.

T-matrix [64] methods have been widely used in optical tweezers modeling. They are particularly suitable to describe optical trapping of composite and arbitrary-shaped particles. Such approach provides a compact formalism based on the multipole expansion of the fields suitable for dealing with scatterers of (almost) arbitrary morphology [22,26], e.g., aggregates of spheres or clusters [18,19,75,76], plasmonic particles [77–79], stratified spheres [80,81], and spheres with internal aggregation (spheres within spheres) [22,82]. The T-matrix approach has been widely used for rigorously computing electromagnetic scattering by single and composite particles. It yields a procedure computationally less intensive than those required by finite elements methods. Moreover, the transformation properties [26,75,83–85] under rotation and translation of the T-matrix make it possible several simplifications in optical force calculations as it requires the T-matrix to be computed only once, with respect to the particle reference frame thus saving much computational time.

For spherical particles, accurate modeling of optical tweezers can be obtained by generalising Mie theory [86] through the so-called generalised Lorenz–Mie theories (GLMTs). In this approach a generic laser beam is expanded on a base of functions, e.g., vector spherical harmonics, and the scattering problem is solved for spheres, so that separation of variables can be used to get the expansion coefficients of the scattered fields [65,87]. The precise connection between the T-matrix formulation and GLMTs can be found in [88], while a description of the use of GLMTs for calculations in optical tweezers can be found, e.g., in [89–93].

2.4. T-matrix methods

In order to calculate radiation forces and torques acting on an optically trapped particle through Eq. (7), we give as an example a description of a T-matrix approach [18]. For simplicity we consider a generic non-magnetic ($\mu = 1$) particle with refractive index n_p in a medium of refractive index n_m illuminated by an incident field $\mathbf{E}_\mathrm{i}(\mathbf{r})$ (the case $\mu \neq 1$ can be treated considering the corresponding multipole expansion of the magnetic fields). The scattered electric field is $\mathbf{E}_\mathrm{s}(\mathbf{r})$, so that the total electric field outside the particle is $\mathbf{E}(\mathbf{r}) = \mathbf{E}_\mathrm{i}(\mathbf{r}) + \mathbf{E}_\mathrm{s}(\mathbf{r})$, while inside the particle is $\mathbf{E}_\mathrm{p}(\mathbf{r})$. The key point of T-matrix methods is the expansion of the fields into a basis of vector spherical harmonics and the consequent application of the boundary conditions across the particle surface [22,26]. The incident, $\mathbf{E}_\mathrm{i}(\mathbf{r})$, and internal, $\mathbf{E}_\mathrm{p}(\mathbf{r})$, fields have to be regular at the origin (fixed inside the scattering particle). Thus, they can be expanded in **J**-multipoles that are a combination of vector spherical harmonics whose radial function is a spherical Bessel function, $j_l(kr)$, ensuring the finiteness at the origin [6,22], e.g.:

$$\mathbf{E}_\mathrm{i}(r, \hat{\mathbf{r}}) = E_0 \sum_{p=1,2} \sum_{lm} W^{(p)}_{\mathrm{i},lm} \mathbf{J}^{(p)}_{lm}(kr, \hat{\mathbf{r}}). \tag{9}$$

where E_0 is the field amplitude, $W^{(p)}_{\mathrm{i},lm}$ are expansion coefficients, the label p is referred to the multipolar components of magnetic ($p = 1$) and electric ($p = 2$) nature and it is linked with parity [83]. In analogy to the incident and internal fields, the scattered wave is expanded in **H**-multipoles, whose radial function is a spherical Hankel function, $h_l(kr)$, of the first kind because the scattered field has to satisfy the radiation condition at infinity [94]:

$$\mathbf{E}_\mathrm{s}(r, \hat{\mathbf{r}}) = E_0 \sum_{p=1,2} \sum_{lm} A^{(p)}_{\mathrm{s},lm} \mathbf{H}^{(p)}_{lm}(k_\mathrm{m} r, \hat{\mathbf{r}}), \tag{10}$$

where $A^{(p)}_{\mathrm{s},lm}$ are the amplitudes of the scattered fields which are determined by imposing the boundary conditions across the surface of the particle. In general, they depend on the orientation of the scattering particle with respect to the incident field. The multipole expansion of the normalized scattering amplitude is obtained by taking the limit of the **H**-multipole fields for $kr \to \infty$ from which the asymptotic form of the scattered field is obtained [22].

The T-matrix of the scattering particle is the operator that, acting on the known multipole amplitudes of the incident field $W^{(p)}_{\mathrm{i},lm}$, gives the amplitudes of the scattered field, $A^{(p)}_{\mathrm{s},lm}$. Because of the linearity of Maxwell's equations and of the boundary conditions, the T-matrix is a linear operator, $\mathcal{T}$, so that $\mathbf{E}_\mathrm{s} = \mathcal{T}\mathbf{E}_\mathrm{i}$. Consequently, if both $\mathbf{E}_\mathrm{i}$ and $\mathbf{E}_\mathrm{s}$ are expanded on suitable bases, $\mathcal{T}$ relates the coefficients of such expansions, encompassing all the information on the morphology and orientation of the particle with respect to the incident field [64]. The transition matrix $\mathcal{T} = \{T^{(p'p)}_{l'm'lm}\}$ of the scattering particle acts on the known multipole amplitudes of the incident field $W^{(p)}_{\mathrm{i},lm}$ to give the unknown amplitudes of the scattered field $A^{(p')}_{\mathrm{s},l'm'}$, i.e.,

$$A^{(p')}_{\mathrm{s},\eta l'm'} = \sum_{plm} T^{(p'p)}_{l'm'lm}\, W^{(p)}_{\mathrm{i},\eta lm}. \tag{11}$$

The quantities $T^{(p'p)}_{l'm'lm}$ take into account the morphology of the particle, but are independent of the state of polarisation of the incident field. Therefore, Eq. (11) holds true whatever the polarisation and it relates the basis-polarised amplitudes of the incident and of the scattered field.

The special case of a homogeneous sphere (Mie theory) of radius a yield a diagonal T-matrix, independent of m, whose coefficients are linked to the Mie coefficients, $a_l = -A^{(2)}_{\mathrm{s},lm}/W^{(2)}_{\mathrm{i},lm}$ and $b_l = -A^{(1)}_{\mathrm{s},lm}/W^{(1)}_{\mathrm{i},lm}$ [22].

By substituting the expansions of the incident Eq. (9) and scattered waves Eq. (10) in terms of multipoles taken in the asymptotic limit ($r \to \infty$), the general expression for the radiation force along the direction of a unit vector $\hat{\mathbf{u}}$, i.e., $F_\mathrm{rad}(\hat{\mathbf{u}}) = \mathbf{F}_\mathrm{rad} \cdot \hat{\mathbf{u}}$ can be obtained [18]:

$$F_\mathrm{rad}(\hat{\mathbf{u}}) = -\frac{\varepsilon_\mathrm{m} E_0^2}{2k_\mathrm{m}^2} \Re \left\{ \sum_{plm} \sum_{p'l'm'} i^{l-l'} I^{(pp')}_{lml'm'}(\hat{\mathbf{u}}) \left[A^{(p)*}_{\mathrm{s},lm} A^{(p')}_{\mathrm{s},l'm'} + W^{(p)*}_{\mathrm{i},lm} A^{(p')}_{\mathrm{s},l'm'} \right] \right\}, \tag{12}$$

where the integrals $I^{(pp')}_{lml'm'}(\hat{\mathbf{u}})$ can be expressed in closed form in terms of spherical harmonics [18]. Note how the force expressed

by Eq. (12) can be separated into two parts related to extinction and scattering terms, $F_{\mathrm{rad}}(\hat{\mathbf{u}}) = F_{\mathrm{ext}}(\hat{\mathbf{u}}) - F_{\mathrm{scat}}(\hat{\mathbf{u}})$, where:

$$F_{\mathrm{ext}}(\hat{\mathbf{u}}) = -\frac{\varepsilon_{\mathrm{m}} E_0^2}{2k_{\mathrm{m}}^2} \Re \left\{ \sum_{plm} \sum_{p'l'm'} W_{\mathrm{i},lm}^{(p)*} A_{\mathrm{s},l'm'}^{(p')} i^{l-l'} I_{lml'm'}^{(pp')}(\hat{\mathbf{u}}) \right\} \tag{13}$$

and

$$F_{\mathrm{scat}}(\hat{\mathbf{u}}) = \frac{\varepsilon_{\mathrm{m}} E_0^2}{2k_{\mathrm{m}}^2} \Re \left\{ \sum_{plm} \sum_{p'l'm'} A_{\mathrm{s},lm}^{(p)*} A_{\mathrm{s},l'm'}^{(p')} i^{l-l'} I_{lml'm'}^{(pp')}(\hat{\mathbf{u}}) \right\} . \tag{14}$$

$F_{\mathrm{ext}}(\hat{\mathbf{u}})$ depends both on $A_{\mathrm{s},lm}^{(p)}$ and on the amplitudes $W_{\mathrm{i},lm}^{(p)}$ of the incident field, while $F_{\mathrm{scat}}(\hat{\mathbf{u}})$ depends on the amplitudes $A_{\mathrm{s},lm}^{(p)}$ of the scattered field only. The subscript are used since this dependence is analogous to that on the extinction and scattering cross sections for the force exerted by a plane wave on a sphere [52]. In fact, the generic expressions for the radiation force are valid for any scatterer and for any direction of the incident field. In the particular case of a linearly polarised plane wave that impinges on a spherical particle, the radiation force is simplified as [52]:

$$\mathbf{F}_{\mathrm{rad}} = \frac{n_{\mathrm{m}}}{c} I_0 \left[\sigma_{\mathrm{ext}} \hat{\mathbf{k}}_{\mathrm{i}} - \oint_{\Omega} \frac{\mathrm{d}\sigma_{\mathrm{scat}}}{\mathrm{d}\Omega} \hat{\mathbf{r}} \mathrm{d}\Omega \right] , \tag{15}$$

in which σ_{ext} and $\mathrm{d}\sigma_{\mathrm{scat}}/\mathrm{d}\Omega$ are the extinction and differential cross-sections, respectively, that can be expressed in terms of Mie coefficients [6], I_0 is the intensity and $\hat{\mathbf{k}}_{\mathrm{i}}$ is the propagation direction of the incident plane wave.

A similar procedure can be followed for the expression of the torque that can be split into extinction and scattering terms [95,96]. Thus, for the axial z-component, $\Gamma_{\mathrm{rad},z} = \mathbf{\Gamma}_{\mathrm{rad}} \cdot \hat{\mathbf{z}} = \Gamma_{\mathrm{ext},z} - \Gamma_{\mathrm{scat},z}$., we have that:

$$\Gamma_{\mathrm{rad},z} = \underbrace{-\frac{\varepsilon_{\mathrm{m}} E_0^2}{2k_{\mathrm{m}}^3} \sum_{plm} m \Re \left\{ W_{\mathrm{i},lm}^{(p)} A_{\mathrm{s},lm}^{(p)*} \right\}}_{\text{extinction}} \underbrace{- \frac{\varepsilon_{\mathrm{m}} E_0^2}{2k_{\mathrm{m}}^3} \sum_{plm} m \left| A_{\mathrm{s},lm}^{(p)} \right|^2}_{\text{scattering}} , \tag{16}$$

where we have explicitly distinguished the extinction and scattering contributions. This relation obtained by Borghese et al. [95,96] is a generalisation of the result obtained by Marston and Crichton [97] for a spherical particle illuminated by a circularly polarised plane wave, for which the longitudinal component of the torque is simply proportional to the absorption cross section, σ_{abs}:

$$\Gamma_{\mathrm{rad},z} = \pm \frac{I_0}{\omega} (\sigma_{\mathrm{ext}} - \sigma_{\mathrm{scat}}) = \pm \frac{I_0}{\omega} \sigma_{\mathrm{abs}}, \tag{17}$$

where the $\pm$ sign is related to left-handed of right-handed helicity of the incident circularly polarised light, respectively. The transverse components of the radiation torque, *i.e.*, $\Gamma_{\mathrm{rad},x} = \mathbf{\Gamma}_{\mathrm{rad}} \cdot \hat{\mathbf{x}}$ and $\Gamma_{\mathrm{rad},y} = \mathbf{\Gamma}_{\mathrm{rad}} \cdot \hat{\mathbf{y}}$, can be calculated in a similar way [6,95], obtaining:

$$\begin{aligned} \Gamma_{\mathrm{rad},x} = & \underbrace{-\frac{\varepsilon_{\mathrm{m}} E_0^2}{4k_{\mathrm{m}}^3} \sum_{plm} \Re \left\{ s_{lm}^{(-)} W_{\mathrm{i},l,m+1}^{(p)} A_{\mathrm{s},lm}^{(p)*} + s_{lm}^{(+)} W_{\mathrm{i},l,m-1}^{(p)} A_{\mathrm{s},lm}^{(p)*} \right\}}_{\text{extinction}} \\ & \underbrace{- \frac{\varepsilon_{\mathrm{m}} E_0^2}{4k_{\mathrm{m}}^3} \sum_{plm} \Re \left\{ s_{lm}^{(-)} A_{\mathrm{s},l,m+1}^{(p)} A_{\mathrm{s},lm}^{(p)*} + s_{lm}^{(+)} A_{\mathrm{s},l,m-1}^{(p)} A_{\mathrm{s},lm}^{(p)*} \right\}}_{\text{scattering}} \end{aligned} \tag{18}$$

and

$$\begin{aligned} \Gamma_{\mathrm{rad},y} = & \underbrace{-\frac{\varepsilon_{\mathrm{m}} E_0^2}{4k_{\mathrm{m}}^3} \sum_{plm} \Im \left\{ -s_{lm}^{(-)} W_{\mathrm{i},l,m+1}^{(p)} A_{\mathrm{s},lm}^{(p)*} + s_{lm}^{(+)} W_{\mathrm{i},l,m-1}^{(p)} A_{\mathrm{s},lm}^{(p)*} \right\}}_{\text{extinction}} \\ & \underbrace{- \frac{\varepsilon_{\mathrm{m}} E_0^2}{4k_{\mathrm{m}}^3} \sum_{plm} \Im \left\{ -s_{lm}^{(-)} A_{\mathrm{s},l,m+1}^{(p)} A_{\mathrm{s},lm}^{(p)*} + s_{lm}^{(+)} A_{\mathrm{s},l,m-1}^{(p)} A_{\mathrm{s},lm}^{(p)*} \right\}}_{\text{scattering}} \end{aligned} \tag{19}$$

where $s_{lm}^{(-)} = \sqrt{(l-m)(l+1+m)}$ and $s_{lm}^{(+)} = \sqrt{(l+m)(l+1-m)}$.

2.5. Focused fields

Finally, to calculate the radiation forces in an optical tweezers we need to consider the multipole amplitudes $\tilde{W}_{\mathrm{i},lm}^{(p)}$ of a highly focused beam. The expansion of a focused beam around the focal point is obtained by exploiting the angular spectrum representation [6,18,90]:

$$\begin{aligned} & \mathbf{E}_{\mathrm{f}}(x,y,z) \\ & = \frac{ik_{\mathrm{t}} f e^{-ik_{\mathrm{t}} f}}{2\pi} \int_0^{\theta_{\max}} \sin\theta \int_0^{2\pi} \mathbf{E}_{\mathrm{ff},t}(\theta,\varphi) e^{i[k_{\mathrm{t},x} x + k_{\mathrm{t},y} y]} e^{ik_{\mathrm{t},z} z} \, \mathrm{d}\varphi \, \mathrm{d}\theta , \end{aligned} \tag{20}$$

in which f is the focal length, k_{t} is the wavenumber transmitted through the objective lens, and each transmitted plane wave, $\mathbf{E}_{\mathrm{ff},\,t}(\theta,\,\varphi)$, can be expanded into multipoles according to Eq. (9). Therefore, the amplitudes of the focused field are:

$$\begin{aligned} & \tilde{W}_{\mathrm{i},lm}^{(p)}(\mathbf{P}) \\ & = \frac{ik_{\mathrm{t}} f e^{-ik_{\mathrm{t}} f}}{2\pi} \int_0^{\theta_{\max}} \sin\theta \int_0^{2\pi} E_{\mathrm{i}}(\theta,\varphi) \, W_{\mathrm{i},lm}^{(p)}(\hat{\mathbf{k}}_{\mathrm{i}}, \hat{\mathbf{e}}_{\mathrm{i}}) \, e^{i\mathbf{k}_{\mathrm{t}} \cdot \mathbf{P}} \, \mathrm{d}\varphi \, \mathrm{d}\theta , \end{aligned} \tag{21}$$

where the centre around which the expansion is performed is considered displaced by $\mathbf{P}$ with respect to the focal point $\mathbf{O}$ and the amplitudes $\tilde{W}_{\mathrm{i},lm}^{(p)}(\mathbf{P})$ define the focal fields and can be numerically calculated once the characteristics of the optical system are known. The expression for the radiation force along the direction of a unit vector $\hat{\mathbf{u}}$, *i.e.*, $F_{\mathrm{rad}}(\hat{\mathbf{u}}) = \mathbf{F}_{\mathrm{rad}} \cdot \hat{\mathbf{u}}$ can be obtained through the knowledge of the scattered amplitudes $\tilde{A}_{\mathrm{s},lm}^{(p)}$ related to the incident focal fields through the particle T-matrix, Eqs. (11). In practice, the expression of the optical force in the focal region is obtained from the correspondent one for the plane wave, Eq. (12), by changing $E_0 W_{\mathrm{i},lm}^{(p)} \to \tilde{W}_{\mathrm{i},lm}^{(p)}(\mathbf{P})$ and $E_0 A_{\mathrm{s},lm}^{(p)} \to \tilde{A}_{\mathrm{s},lm}^{(p)}$ [18].

2.6. Size scaling in optical trapping for spherical particles

As application of the T-matrix approach we investigate the size scaling of the optical trapping for non-absorbing polystyrene spheres. Size scaling is a paradigm of nanoscience [98] as it characterises condensed matter systems for many applications in the most different research fields [99]. Crucial properties of materials and interactions change dramatically with size [100] influencing a wide variety of technological applications [101]. The size scaling properties of optical forces help us understand the important features of optical trapping in a wide size range and their comparison with experiments [102].

Polystyrene spheres are a typical sample used in optical tweezers experiments since they are easily purchased in accurate spherical shape and are used as size standard in microscopy techniques. They are easily functionalised and are well suited for optical tweezers applications in a biological environment [13]. Thus, they often represent the standard sample used for optical force calibration in optical tweezers [6,102]. The particle refractive index is

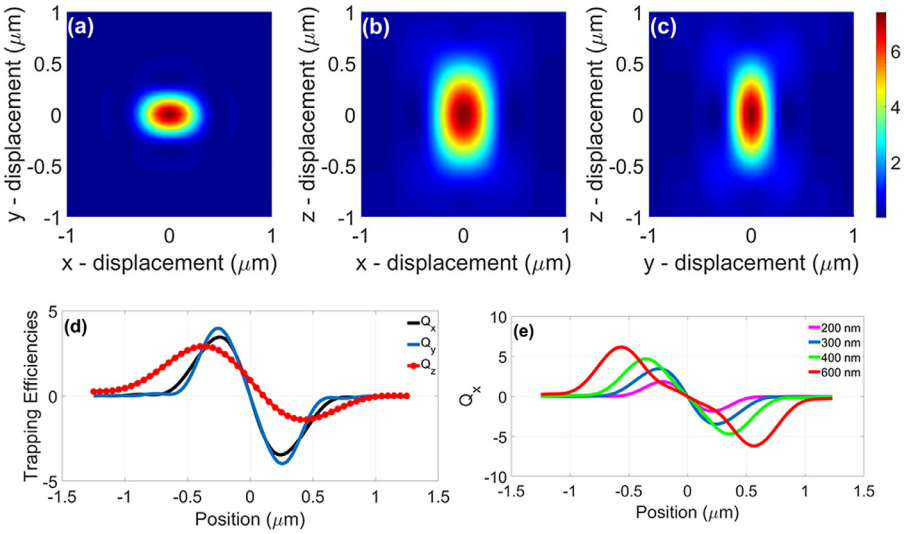

Fig. 1. The figures (a), (b) and (c) are maps of the focused field intensity normalized to the field entering the objective lens in the *xy* (a), *xz* (b), and *yz* (c) planes. We have considered a strongly focused field (NA = 1.3) that is linearly polarised along *x* and propagates along the *z* direction. Therefore, in the *xy* plane the cylindrical symmetry of the intensity map is broken by the polarisation, while in *xz* and *yz* planes the shape of the field appears elongated because of the beam propagation. With this incoming field, in the figure (d), the trapping efficiencies (Q_x, Q_y, Q_z) for a polystyrene ($n_p = 1.57$) sphere (radius of 300 nm) immersed in water ($n_m = 1.33$) are graphed in the transverse *x, y* (black and blue lines respectively) and longitudinal *z* (red line and dots) directions, as function of the particle displacement from the nominal paraxial focus. In (e), we compare the trapping efficiency along *x* direction for spheres of different radii: 200 nm (magenta line), 300 nm (blue line), 400 nm (green line) and 600 nm (red line). (For interpretation of the references to color in this figure legend, the reader is referred to the web version of this article.)

$n_p(\lambda_0 = 830\ \text{nm}) = 1.57$ [103]. We fix the wavelength of the linearly polarised trapping laser beam at $\lambda_0 = 830$ nm and we consider the particles immersed in water ($n_m = 1.33$). We consider a Gaussian laser beam focused by an ideal aplanatic lens which does not absorb and does not produce any aberration. The numerical aperture of the objective lens is taken as NA= 1.3.

We are interested in the exact calculation of optical forces, related trap stiffnesses, their scaling with particle size, and comparison with dipole approximation and ray optics calculations. We cover a wide size range with particle radius ranging from 50 nm up to 1.4 μm. Therefore, the size parameter range is $[0.5 - 14.1]$ and only at the extreme values of the considered interval ray optics or dipole approximation calculations are safe to be used. This is indeed the typical size range of optical tweezers experiments [6]. The direction of propagation of the beam is taken along *z* and the polarisation axis along *x*.

A graph of the calculated strongly focused incident field intensity is provided in Fig. 1a–1c. In these field intensity maps it is evident how the most elongated region is along the propagation (axial) direction, *z*, as expected for a focused Gaussian beam. Moreover, in the *xy* plane the linear polarisation of the incident beam breaks the cylindrical symmetry in the focal plane producing a tighter spot size along *y* with respect to the polarisation direction, *x*. This has observable consequences also on the symmetry of the optical trap and the transverse stiffnesses, κ_x and κ_y, particularly when dealing with nanostructures [10,20,104].

Within the T-matrix approach we have computed the (*x, y, z*) components of the optical force on the points of a computational grid employed with appropriate resolution. These components are calculated in a micron-sized range, [−1.4 μm,1.4 μm], around the paraxial nominal focus of the beam. So, we can plot the force as a function of particle displacement in each spatial direction, *x, y, z*. The trapping position of the particle in the longitudinal (*z*) direction is typically offset from the centre of the coordinate system due to the offset of the optical scattering force. To calculate the transverse force on the particle at the equilibrium position, the *z* (longitudinal) coordinate at which the axial force vanishes must first be found. The force plots in the transverse directions (*x, y*) can then be calculated. It is often convenient to calculate the dimensionless force efficiencies along the three cartesian directions, $Q_i = cF_i/n_m P$ with $i = x, y, z$. In Fig. 1d we show them as calculated for a polystyrene sphere with radius $a = 300$ nm. The graphs present a relative maximum and minimum approximately at the particle radius. As expected, it is here at these extremal points that the greatest restoring force is exerted because these correspond to the maximum light intensity gradient. For this particular particle size ($a = 300$ nm) the sphere occupies approximately the entire focal region yielding an optimum in the trapping strength. To confirm this, we can study the trend of trap efficiencies as the radius changes, e.g., for Q_x, Fig. 1e. Indeed, for larger dimensions of the particle, the slope of the curves gets smaller around the equilibrium point. The reason is that for larger particles the volume of the particle exceeds the interaction volume related with the laser spot, and the corresponding stiffness tends to zero as the particle radius increases.

In proximity of the equilibrium point the optical force can be linearized as an elastic restoring force with negative slope, e.g., $F_x \approx -\kappa_x x$ for the *x*-direction. Thus, optical tweezers can be approximated with an effective harmonic potential with spring constants or trap stiffnesses κ_x, κ_y κ_z. These quantities are of crucial importance in experiments because represent quantities measured when performing optical tweezers calibration [105]. In order to calculate the optical trap stiffnesses, we simply get the slope of the force-displacement graphs at the equilibrium position, where the force vanishes. In Fig. 2a–2c we show the calculated stiffnesses as a function of particle radius, *a*.

In the three graphs, an absolute maximum is present corresponding to a radius of $a \approx 300$ nm. This is the radius for which the volume of the scatterer overlaps the laser spot, optimizing the interaction region [27,28]. However, the peak in the axial direction, Fig. 2c, is more depressed than in the transverse ones, see Fig. 2a and 2b. This is due to the shape of the focal spot shown in Fig. 1a–1c, representing the maps associated with the incident field, which show a tighter profile in the transverse direction than

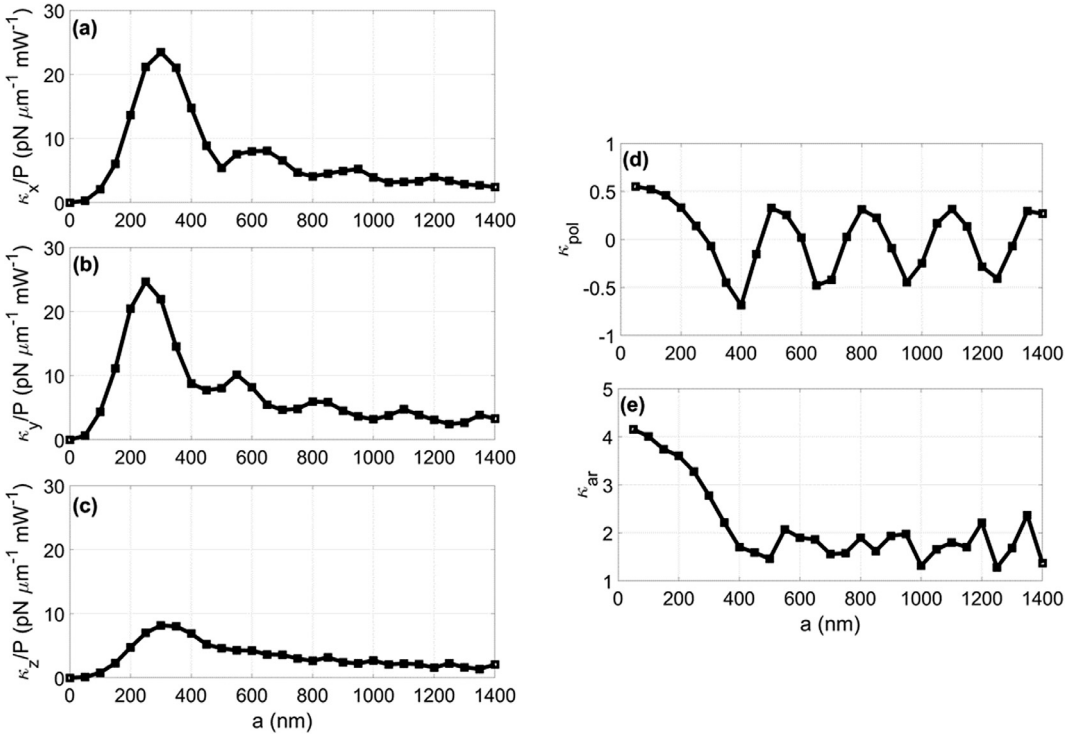

Fig. 2. Optical trap stiffnesses, κ_x (a), κ_y (b), κ_z (c), for a polystyrene ($n_p = 1.57$) sphere immersed in water ($n_m = 1.33$) in the transverse, x (a) - y (b), and longitudinal z (c) directions, as a function of the particle radius a. The figures (d) and (e) show, respectively the polarisation anisotropy, κ_{pol}, and trap aspect ratio, κ_{ar}, as a function of a. The radius of the considered spheres spans in the interval [50 nm–1400 nm]. The symbols, excluding zero, are the calculated points by a T-matrix approach.

in the axial one, yielding a tighter effective potential and a larger stiffness in x, y with respect to z. For size larger than the one corresponding to this maximum, the scaling of the force constants follows a hyperbolic scaling behaviour, $\kappa \propto a^{-1}$, this is also consistent with calculations in the ray optics approximation [6], blue lines in Fig. 3a and 3b. Using the T-matrix approach, we can reproduce the full electromagnetic theory of optical forces with great precision. In fact, when particles become larger than the interaction region, we also find the onset of modulation in the stiffnesses caused by the interference between the different multipoles [27,28]. An exhaustive explanation of the interplay between the multipole interference for mesoscale particles is described by Nieminen et al. [29]. In fact, the gradient force from which we obtain the trap stiffnesses appears to be only weakly affected by this interference and good agreement between T-matrix and ray optics calculations is found for values of particle size well below the typical ray optics validity range ($x \gtrsim 50$) [27–29]. Note that this agreement is not occurring for other relevant quantities such as the scattering force where ray optics (that by definition neglects interference effects) fails to predict its strong variation with size and it only yields an average value [29].

On the other hand, for smaller values, the behaviour of the trap constants increases with a cubic power law, $\kappa \propto a^3$, in agreement with the volumetric scaling of the particle polarisability in the dipole approximation. As an example, in Fig. 3a, we compare the scaling of the transverse stiffness, κ_x, calculated with the T-matrix approach, Fig. 2a, with what is analytically obtained by a dipole approximation and considering a diffraction limited Gaussian beam spot. In our analytical calculation, the paraxial Gaussian beam waist w_0 is provided by the Abbe criterion [33,106] so that $w_0 = 0.5\lambda_0/\mathrm{NA}$. As shown by a logarithmic scale plot in Fig. 3b, the comparison between values calculated in dipole approximation and T-matrix is very good up to 200 nm. The same type of comparison and considerations hold for the size scaling of κ_y and κ_z. Such behaviour has been experimentally verified by measuring trap stiffnesses in a wide range of particle size from nano to the microscale [102].

Finally, in Fig. 2d and 2e we represent respectively the polarisation anisotropy, $\kappa_{pol} \equiv 1 - \kappa_x/\kappa_y$, and the aspect ratio $\kappa_{ar} \equiv (\kappa_x + \kappa_y)/\kappa_z$. These quantities are related to both laser beam (polarisation, propagation) and particle properties (size, shape, asymmetry) and can be easily measured in experiments and linked to theoretical predictions [20,102,104].

3. Experimental practice

An optical tweezers setup is an ideal tool to trap and manipulate micro and nanoparticles in liquid solutions with nanometer accuracy and to measure and apply piconewtonian forces [14]. Experimentally, optical trapping is achieved by focussing a laser beam to the diffraction limit by an objective lens with a high numerical aperture. For this reason optical tweezers setups are usually realized coupling a laser light source with an optical microscope, where the objective is also used to image the sample on a camera. An optical tweezers setup can be based on different kinds of optical microscopes: normal or inverted, commercial or customized, according to user requirements and budget. Usually, customized microscopes have lower costs and a bigger flexibility compared to commercial ones. Furthermore, more stable traps are obtained using optical tweezers based on inverted microscopes, because the laser beam is directed upwards and gravity works in an opposite direction to the radiation pressure. Since the realization of the first single-beam optical tweezers in 1986 [5], several technologies have been developed and merged with optical tweezers to customize setups for several purposes [105]. Currently, thanks to the new generation of digital sensors it is possible to investigate phenomena having spatial and time scales not reachable until few years ago. Liquid crystal displays (LCDs) with high resolution have been employed as reflective elements in holographic optical

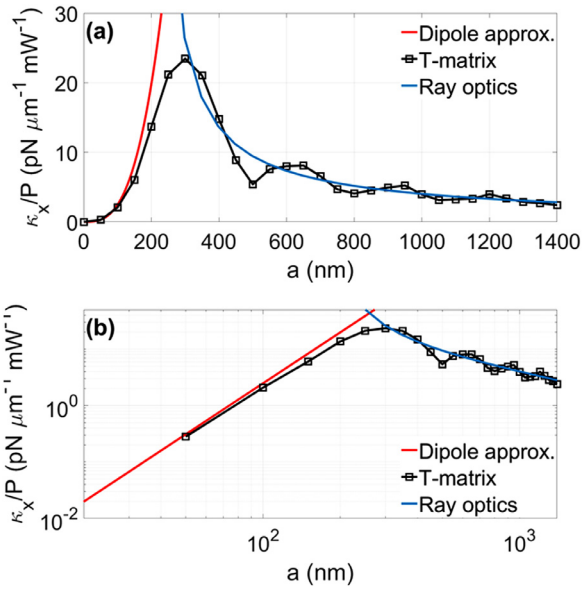

Fig. 3. Optical trap stiffnesses along the x-direction for a polystyrene ($n_p = 1.57$) sphere immersed in water ($n_m = 1.33$) as a function of the particle radius a. The radius of the considered spheres spans in the interval [50 nm–1400 nm]. The black data are obtained using the T-matrix approach. The red line is, instead, referred to the dipole approximation calculations considering a diffraction limited Gaussian beam. While the blue line represent optical trapping calculations in the ray optics approximation. In (a) we show a linear scale plot, while in (b) we show the same data in logarithmic scale to explicitly follow the size scaling. (For interpretation of the references to color in this figure legend, the reader is referred to the web version of this article.)

tweezers (HOT) to shape laser beams. In doing this, it is possible to create and move multiple traps in real time and to generate vector beams able to carry optical spin and angular momentum [108]. Furthermore, real time tracking and feedback position systems are now available [109]. Although there are several kinds of optical tweezers setups, their principle of operation can be understood by considering a standard optical tweezers setup Fig. 4. This is a forward-scattering setup mounted around an inverted microscope. A laser source generates a collimated beam, which is expanded by a telescope lens system and reflected by a dichroic mirror to overfill the back aperture of an oil immersion objective having an high numerical aperture. The overfilling creates the maximal optical field gradient in the focal spot for a more efficient trapping. The dichroic mirror acts like a short pass filter, it reflects the laser light and transmits the visible light to a camera, preventing the saturation of the CMOS detector and allowing the view of the sample on a monitor. The sample is held and moved by micrometric translational stage mounted on an inverted microscope. Forward scattered light from trapped particle is collected by a condenser and reflected by a dichroic mirror to a quadrant photo detector (QPD) [6]. Thus, particle tracking and optical tweezers calibration can be achieved either by video microscopy either by photonic force microscopy, i.e., by the temporal or frequency analysis of the light scattered onto the QPD. Digital video microscopy is based on the analysis of the images from a digital camera to track the trajectories and displacements of the imaged objects with a subpixel resolution and a sampling rate depending on the camera performances [110]. Photonic force microscopy allows to track the displacements of a single trapped particle, using a photodetector, with a typical spatial resolution of 0.1 nm and sampling rate above 100 kHz [111].

3.1. Optical tweezers calibration

The main goal of calibrating an optical tweezers is to determine their trap stiffness κ and to measure the absolute displacements of the trapped particles. For small displacements from the equilibrium position (e.g., along x axis), the trapping potential is considered to be harmonic with a Hookean restoring force $F_x = -\kappa_x x$ and potential energy $E_x = \frac{1}{2}\kappa_x x^2$ (we will refer only to the x component in order to shorten the notation). In doing this, once the trap stiffness κ_x is known, the x component of an external force acting on the particle can be quantified by measuring the particle displacement x. For spherical particles measuring these three stiffnesses, κ_x, κ_y, κ_z, fully characterise the optical trap. However, this is strictly valid for spherical particles where only translational degrees of freedom can be considered. For non-spherical particles optical torque, polarisation, and angular fluctuations play a role and must be included in the calibration analysis and the reconstruction of the effective trapping potential [20,21,45,104,107,112] (see for example Fig. 5). In fact, the dynamics of non-spherical particles in optical traps can be very complicated due to the occurrence of transverse components of the scattering force and optical torques [54,56]. For example elongated rod-shaped (e.g., nanowires) or ellipsoidal particles align with the optical (z-)axis of the trap (see Fig. 4) due to the optical torque and show small angular thermal fluctuations about their stability axis that can be measured together with optical aligning torques [20,104]. Moreover, the translation-rotation coupling in non-spherical particles can yield regular biased orbital motion that has been the subject of recent experimental and theoretical investigations [107,113–116].

Typical optical tweezers setups, use cameras or photo-detectors to detect the motion of trapped particles. In both cases, their measurements units (pixels and volts) are proportional, by a calibration constant and around the equilibrium position, to the absolute particle displacement [6,117]. There are several active or passive calibration protocols, but here we briefly discuss only the most common passive ones as applied to spherical particles: potential analysis, autocorrelation function analysis, power spectrum and mean square displacement analysis [6,117]. The simultaneous application of different calibration methods is a good check to confirm their consistency and the quality of the acquired experimental data. Spatial calibration with digital video microscopy is easier than QPD since it is possible to image directly reference targets having well know dimensions to find the conversion factor pixel/μm. Once this factor is known it is possible to proceed to the force calibration.

Optical potential method.– Considering the Brownian motion of a trapped particle Fig. 5a it is possible to calculate its positional distribution functions $\rho(x)$ Fig. 5b. This can be used to determine the profile of the trapping potential $U(x) = k_B T \log \rho(x)$ Fig. 5c. In doing this, the trap stiffness κ_x can be obtained as fit parameter of the potential $U(x)$ Fig. 5c.

Autocorrelation method.– In this case the starting point of the calibration procedure is the Langevin equation describing displacement $x(t)$ of an optically trapped particle in liquid solution [118–120]:

$$m\frac{d^2x(t)}{dt^2} + \gamma\frac{dx(t)}{dt} + \kappa_x x(t) = F_x(t), \tag{22}$$

where $\gamma\frac{dx}{dt}$ is the viscous damping term, $\kappa_x x(t)$ is the restoring force term, $F_x(t)$ is a random fluctuating force and γ is the hydrodynamic viscous coefficient related to the medium viscosity η and to the particle size and shape, which for spherical particles with radius r becomes $\gamma = 6\pi\eta r$, according to the Stokes law. In the low Reynolds number limit, applicable to microparticles suspended in water, the system can be considered overdamped and the first term of Eq. (22) can be neglected when compared to the others. In this special case, the particle motion $x(t)$ can be well described by

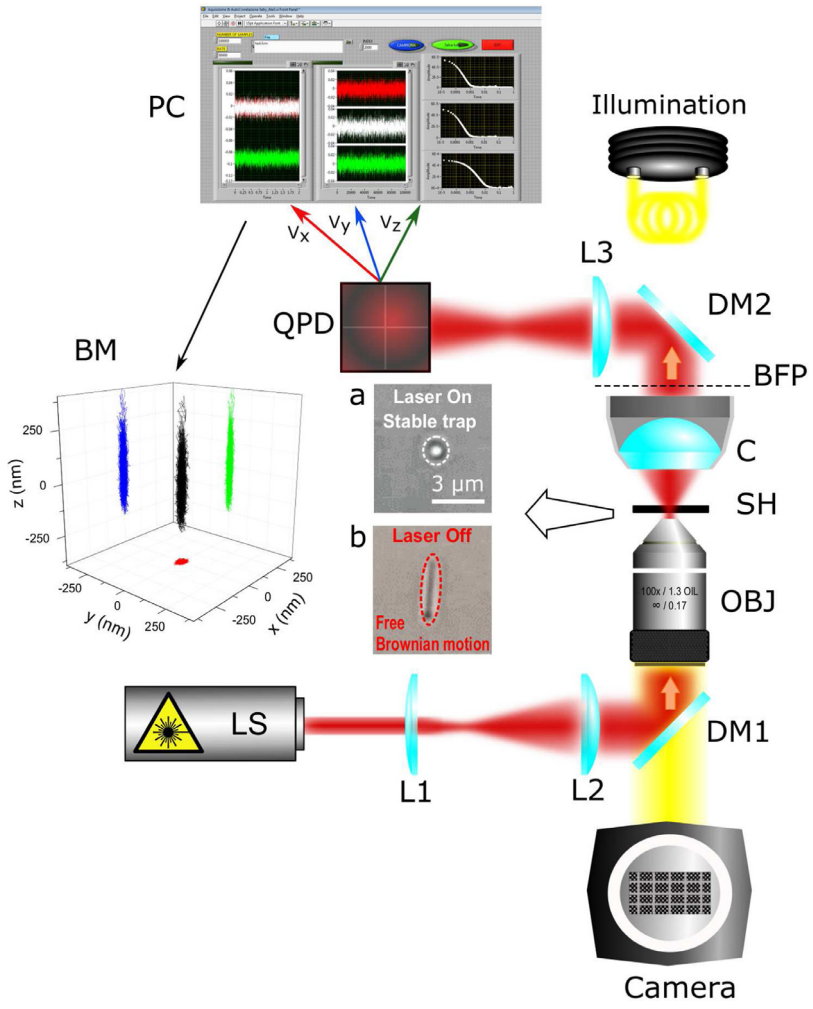

Fig. 4. Scheme of a typical OT setup. Trapping is achieved by a tightly focussed laser beam using a high-numerical-aperture objective lens (OBJ), which is also used to image the sample on a camera. The beam produced by the laser source (LS) is enlarged through a telescope lens system (lenses L1 and L2) to overfill the back aperture of the objective. A dichroic mirror (DM1) is used to reflect the laser light to the objective and to transmit the visible light to the camera. The sample is held and moved by a sample holder (SH). Inset (a) represents the real image of a SiNW optically trapped and aligned along the propagating axis of the laser beam [20,107]. When the laser is switched off the SiNW performs Brownian motion and its alignment is randomized. Scattered and transmitted lights are collected and overlapped by a condenser lens (C) and projected on a QPD by a second dichroic mirror (DM2) and a lens (L4). Signals from the QPD are analyzed by a PC in order to calculate the calibration factors and to reconstruct the 3D Brownian motion of the trapped sample.

the overdamped Langevin equation:

$$\frac{dx(t)}{dt} + \omega x(t) = \xi_x(t), \tag{23}$$

where $\xi(t) = \frac{F(t)}{\gamma}$.

This equation can be properly recast to determine the analytic expression of $C_{xx}(\tau)$, which is the autocorrelation of the displacement $x(t)$ [6,117]. In particular, for a spherical particle $C_{xx}(\tau)$ decays exponentially with a characteristic time τ dependings on the trap spring constant κ_x and on the hydrodynamic drag coefficient γ [121]:

$$C_{xx}(\tau) = C_{xx}(0) \exp\left(-\frac{\kappa_x}{\gamma}\tau\right) \tag{24}$$

Since the QPD produces voltage signals $V_x(t) = \beta_x x(t)$ proportional by the position calibration factor β_x to $x(t)$, the autocorrelation function of the experimental displacements can be expressed as $C^V_{xx}(\tau) = \langle V_x(t)V_x(t+\tau)\rangle = \beta_x^2 C_{xx}(\tau)$, where according to the equipartition theorem $C^V_{xx}(0) = \beta_x^2 C_{xx}(0) = \beta_x^2 k_B T/k_x$ and the calibration factor β_x can be expressed as:

$$\beta_x = \sqrt{\frac{C^V_{xx}(0)\kappa_x}{k_B T}} \tag{25}$$

The experimental autocorrelation function $C^V_{xx}(\tau)$ can be fitted by Eq. (24) to obtain the stiffness κ_x which, together with the experimental value of $C^V_{xx}(0)$, are employed to calculate the calibration factor β_x according to the Eq. (25).

Power spectrum method.– The power spectral density (PSD) of a signal, describing how its energy is distributed with frequency, can be also employed to calibrate optical tweezers. Considering the Fourier transform of the overdamped Langeven equation Eq. (23):

$$-i\omega\tilde{x}(\omega) + \omega_x\tilde{x}(\omega) = \tilde{\xi}_x(\omega), \tag{26}$$

where we defined $\omega_x = \kappa_x/\gamma$ and solved for $\tilde{x}(\omega) = \tilde{\xi}_x(\omega)/(-i\omega + \omega_x)$.

The corresponding power spectrum shows a Lorentzian profile:

$$S_x(\omega) = |\tilde{x}(\omega)|^2 = \frac{2D}{\omega^2 + \omega_x^2}, \tag{27}$$

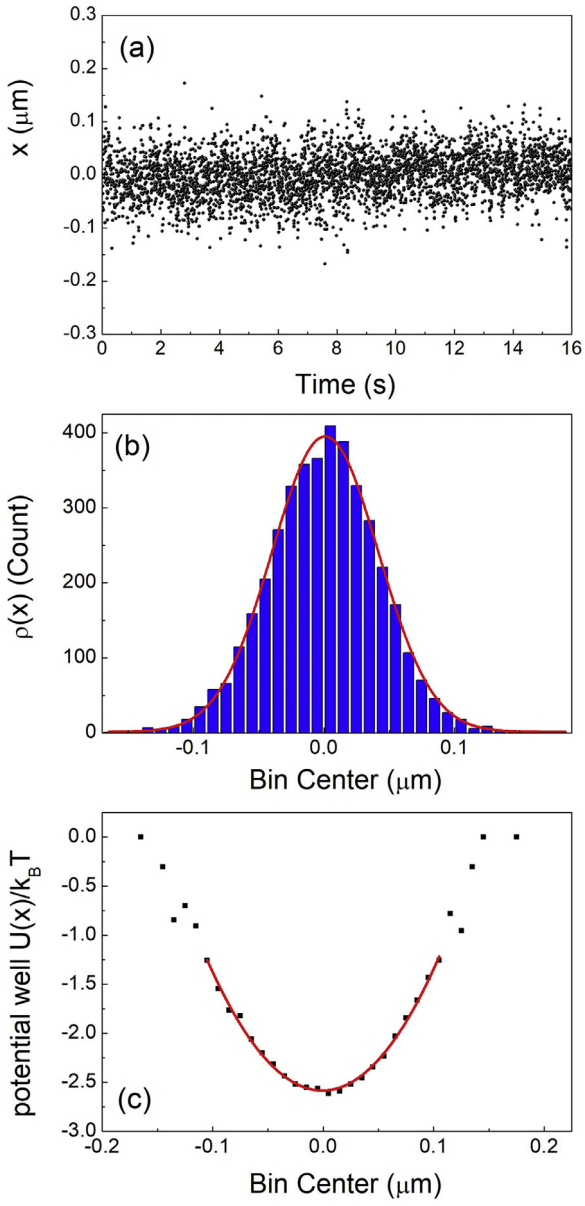

Fig. 5. Data analysis for a SiNW with a diameter of 10 nm and a length of 3.6 μm. (a) x component of Brownian motion. (b) Probability distribution function $\rho(x)$. (c) Potential well profile of the trap $U(x)$. Red lines represents a quadratic fit, from which the trap stiffness κ_x can be calculated as fitting parameter. (For interpretation of the references to color in this figure legend, the reader is referred to the web version of this article.)

where the half-width of the distribution is the relaxation frequency of the trap ω_x. By fitting the power spectrum of the signal, it is possible to obtain the corner frequency ω_x as fit parameter and hence deduce the trap spring constant κ_x. Also in this case the power spectrum of the signal from a QPD is proportional to the power spectrum of the particle fluctuation:

$$S_x^V(\omega) = \beta_x^2 S_x(\omega) = \beta_x^2 \frac{2D}{\omega^2 + \omega_x^2} \tag{28}$$

Setting $\omega = 0$ the calibration factor β_x can be expressed as:

$$\beta_x = \sqrt{\frac{S_x^V(0)\omega_x^2}{2D}} \tag{29}$$

Mean square displacement.– This calibration method is based on the analysis of the mean square displacement (MSD) of the trapped particle: a measure of the deviation of the particle position from its initial position in a time interval τ [117,122]:

$$\mathrm{MSD}_x(\tau) = \langle [x(t+\tau) - x(t)]^2 \rangle = 2\frac{k_B T}{\kappa_x}\left[1 - e^{-\omega_x|\tau|}\right]. \tag{30}$$

Considering this equation it is possible to notice that $\mathrm{MSD}(0) = 0$, $\mathrm{MSD}(\tau)$ presents a transition from a linear growth corresponding to a free diffusion behaviour at low short time scale ($\tau \ll \omega_x^{-1}$) to a plateau value of $2\frac{k_B T}{\kappa_x}$ for $\tau \gg \omega_x^{-1}$, due to the particle confinement at long timescales. Also in this case the MSD of the QPD signals is proportional to that of the particle displacements, $\mathrm{MSD}_x^V(\tau) = \beta_x^2 \mathrm{MSD}_x(\tau)$. Combining the relations above and setting $\tau \to \infty$ we get $\mathrm{MSD}_x^V(\infty) = 2\beta_x^2 / \frac{k_B T}{\kappa_x}$ from which the calibration factor can be calculated as:

$$\beta_x = \sqrt{\frac{\mathrm{MSD}_x^V(\infty)\kappa_x}{2k_B T}} \tag{31}$$

It is noteworthy that all the calibration methods used to calibrate optical tweezers based on photodetectors, can be also applied to camera ones, in this case instead of volt there will be pixel units.

4. Applications

In this section we give an overview of some recent applications of optical tweezers and optical forces in liquid environment. The contactless manipulation of particles promotes the use of OT in a wide variety of research fields. Here, we describe a selection of systems where OT has enabled advances in biology, microbubbles manipulation, chiral optomechanics, nanotechnology, optical binding, spectroscopy, critical Casimir forces, stochastic thermodynamics, and active matter.

4.1. Mechanical properties of red blood cells

Optical tweezers have numerous applications in biological sciences, ranging from single molecule studies [123,124] to cell biophysics [125,126]. In this section we will consider one particularly successful application, namely the investigation and determination of the mechanical and elastic properties of red blood cells (RBCs). Very early in the history of optical tweezers Ashkin et al. showed that RBCs (and many other biological species) could be trapped without optical damage using and infra-red laser beam [11]. Subsequent experiments aimed at determining mechanical properties of RBCs have used both the direct trapping method, or applied forces to the cell indirectly using optically trapped microbeads bound to the cell as 'handles'. The first method has the advantage of simplicity of set-up and sample preparation, in the second calibration of the applied forces is more straightforward.

Hénon et al. attempted to determine the shear modulus of the RBC membrane by stretching cells using microbead handles in calibrated optical traps [127]. Experiments were performed on cells in the native biconcave discoid shape, and cells that were osmotically swollen to a spherical shape, which permitted an exact algebraical solution to the deformation geometry. In both cases for applied forces below 15 pN a linear (with increasing force) deformation of the cell was observed, producing a shear modulus of $\mu = 2.5 \pm 0.4\ \mu\mathrm{N}\cdot\mathrm{m}^{-1}$. At higher applied forces the cell entered a nonlinear deformation regime. Later, Dao et al. [128] used the same experimental geometry in a system capable of applying much higher forces of up to 340 pN. These experiments were complemented by computed simulations, and suggested that at high applied stress where deformations as large as 50% were observed, the membrane shear modulus could be as high as $\mu = 11.1\ \mu\mathrm{N}\cdot\mathrm{m}^{-1}$

Bronkhorst et al. showed that optical tweezers could be used to deform a red blood cell under direct trapping using a line of three

optical traps to 'fold' the cell and observe the relaxation time [129]. Later Liao et al. showed that RBCs could also be stretched under direct trapping, using a single beam that jumped rapidly between two locations to grip the cell [130]. As the separation between the two trap locations was increased the cell was stretched along the line joining them. In this work the elongation of the cell was explained qualitatively using a two-dimensional model. Later theoretical work accurately calculated the optical stress distribution over the surface of an RBC osmotically swollen to adopt a spherical shape and its resulting deformation in the dual tweezers stretching experiment [131]. By solving for the dynamic deformation of the RBC, that is, accounting for the change in shape and redistribution of optical stress as the cell deforms towards the stretched state the authors could determine the membrane mechanical properties (Young's modulus and shear modulus) before and after treatment with N-ethylmaleimide, which is known to cause a decrease in cellular deformability. This work was further refined for the RBC in its native biconcave discoid shape [132]. When predicting the deformation of the RBCs under optical stress it is necessary to account for both the non-linear [133,134] and viscoelastic [135] properties of the cell. By combining optical tweezers stretching with Raman spectroscopy, Raj et al. found that at large deformation the RBC must undergo a structural transformation in order to bear the high load [136].

An alternative technique for deforming cells using optical forces is the optical stretcher [137]. Rather than using strongly focused laser beams as is the case in optical tweezers, the optical stretcher employs two weakly diverging counter-propagating beams to trap particles. The distribution of optical stress over the surface of the trapped object leads to elongation along the beam propagation axis [137]. When complemented by deformation modelling [138,139], the optical stretcher can be used to quantify cell mechanical properties in a high throughput manner [140] as the cells flow in a microchannel through the stretching beams rather than being captured individually in optical tweezers. In some situations, extreme stretching can give rise to irrecoverable shape changes of the cell into a so-called "columnar" form [141].

Altered mechanical properties of RBCs has been linked with a number of pathological conditions [142,143], and optical tweezers have been used to test several of these including malaria (*plasmodium falciparum*) [144,145], diabetic retinopathy [146] and birdshot chorioretinopathy [147]. Similarly optical tweezers have been used to show that the drug Atorvastatin softens the RBC membrane [148].

4.2. Microbubbles

Optical trapping of gas microbubbles presents additional challenges due to their buoyancy, and to their refractive index which is lower than the suspending medium. Due to their low relative refractive index the optical gradient force acts to repel them from the high intensity part of a laser beam and consequently alternative strategies are needed for optical trapping. One possibility is to use a Laguerre-Gaussian (LG) beam [149] whose annular intensity profile provides transverse confinement of the bubble to the beam's dark core. In the vertical direction the position of the bubble is determined by the balance between optical forces and buoyancy, and so the LG beam does not form a three-dimensional optical trap. When implemented in an upright microscope with the trapping LG beam propagating downwards it is a form of 'counter-levitation'. Three-dimensional optical trapping requires the addition of a second counter-propagating hollow beam [34]. In principle, structured light such as optical bottle beams [150] can be also used for three-dimensional optical trapping of microbubbles.

A second strategy is to use a 'time-averaged' optical trap, created by scanning a focussed Gaussian around the circumference of the microbubble. If the scanning frequency is high enough, that is, if the beam rotates around the bubble faster than it can diffuse away then the bubble remains trapped on the axis of rotation [151]. Such a trapping scheme was implemented in an upright microscope, and the dependence and scaling of the trapping force on the bubble radius and radius of the trap beam scanning circle has been investigated [152]. A theoretical analysis of the optical forces in this configuration [153] has shown that that there is a sufficient optical gradient force in all directions to provide a restoring force on the bubble, and hence it is a true three-dimensional optical trap. Indeed, the axial gradient force can be enough to confine a microbubble in an inverted microscope optical tweezers [154].

Microbubbles are also amenable to trapping using acoustic fields. The combination of acoustic and optical trapping presents a great advantage in the differing length scales over which they operate: the acoustic field may be used for long-range manipulation before an optical trap is used for high-resolution control of position [155]. The optical and acoustic traps also complement each other as, once calibrated [156], the optical trap may be used to measure the acoustic forces on the bubble [157]. Such a system may be used to characterise an individual microbubble, and in particular its acoustic response, with a view to reducing the uncertainties from population averaging [158]. Further applications of optically trapped of microbubbles include Raman spectroscopy of the gas enclosed by the bubble [159], measuring the microbubble shell thickness [160], and positioning the bubble adjacent to cells prior to it being irradiated by ultrasound. The cells may then be damaged or destroyed by the oscillations and subsequent collapse of the microbubble [161].

4.3. Chiral optical forces

Chirality derives from the lack of mirror symmetry of an object. A chiral object exists in left- and right-handed version (enantiomers) that cannot be superimposed by translations and rotations within the space where they are embedded. Also circularly polarised light is chiral, with handedness depending on the electric field sense of rotation with respect to the propagation axis. Besides linear momentum, circularly polarised light may transfer also spin angular momentum [162]. Recently, several works considered chirality-dependent optical forces on small particles aiming at all-optical separation of enantiomers [163–165]. The optomechanical interaction of chiral light with mesoscopic objects has been studied in optical tweezers, giving the opportunity to investigate the transfer of spin angular momentum to birefringent particles and observe spin-dependent light-induced rotations [166–169]. Chiral optomechanics on supramolecular chiral particles has been recently investigated on cholesteric liquid crystals (CLC) [170–174]. In particular, left-handed CLC solid microparticles have been synthesized [175], optically trapped, and chiral rotations observed for the corresponding left-handed circularly polarised light [176,177]. In fact, the left-handed CLC particles behave as chiral mirrors, which reflects only left-handed light, while maintaining its handedness [176]. On the contrary, right-handed light is transmitted unaffected. Due to the conservation of angular momentum, a reaction torque is transferred from the circularly polarised trapping beam to the chiral microparticle [176]. In case of microparticles in the low chirality regime [178], an additional contribution to the optical torque due to residual birefringence must be taken into account to fully explain the rotation dynamics of trapped CLC particles at variable degree of ellipticity of the trapping beam [177]. The combination of chiral and optical retardance properties allows to better control the optomechanics of these microparticles that open perspectives for the study of chiral optical sorting, laser trapping and cooling of chiral mesoscopic particles based on the cou-

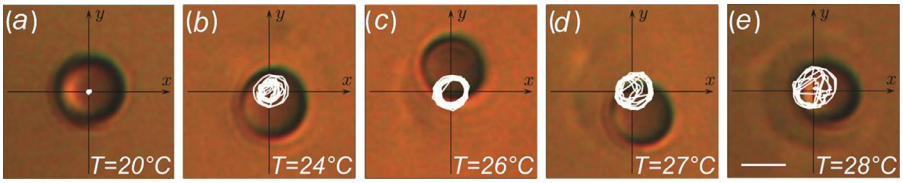

Fig. 6. Micro-engine powered by critical demixing. An optically trapped colloidal particle, with radius $a = 1.24$ μm, immersed in a water–2.6-lutidine critical solution performs rotations around the trapping beam. The performances of the engine can be tuned by adjusting the criticality of the mixture via the ambient temperature. At low temperature (a), the particle is stably trapped. When the temperature increases (b), the particle starts to rotate around the optical beam (white solid lines trajectories), reaching its maximum value for a temperature of 26° (c) with a very reproducible trajectory. A further increase of the temperature results in a decrease of the engine rotations and performances (d, e). The white bars in (e) correspond to 1 μm. Figure adapted from Schmidt et al. [179]

pling of their translational and rotational degrees of freedom, and microcavity optomechanics, by embedding at the centre of the chiral microparticle a resonant nanoparticle.

4.4. Nanotechnology applications

During the last few decades much effort has gone into the miniaturization of machines down to microscopic scales, often inspired by biological systems [180]. This miniaturization process is crucial for the development of nanotechnology [181] and, in this context, optical tweezers are a powerful tool to assemble micro- and nanodevices thanks to their ability of contactless manipulation [10,182,183]. Moreover, they are capable of applying and detecting extremely small (femtonewton) forces and torques yielding potential for driving nanomachines [184–187]. At the nanoscale, semiconducting [20,21,45,104,185,188], metal [125,189–194], and hybrid [78,81] colloidal particles have been trapped and manipulated opening novel exciting possibilities for assembly, characterisation and optical control of nanodevices and biomolecules [10].

Nanodevices or micro-engines need power to operate and to be controlled. A solution to this demand can be provided by structured optical beams, carrying orbital and spin angular momentum (SAM and OAM), generated by holographic optical tweezers (HOT) or similar techniques [195]. In particular, microrotators and micropumps have been realized by transferring SAM and OAM to microparticles [166,176,177,196,197].

Another approach to power nanodevices is to emulate the working principles of heat engines. The nucleation of vapour bubbles inside silicon micro-cavities has been used to realize several microscopic heat engines with a working volume of only 0.6 mm^3 [198,199]. Also, a micro-particle has been employed as a piston in an optical tweezer, realising a microscopic steam engine powered by the periodic generation of cavitation bubbles [200]. Microscopic versions of the Stirling and Carnot cycles have been realized using optically trapped particles to study their stochastic thermodynamic properties [201,202]. Recently, a microscopic engine powered by the density fluctuations of a critical solution has also been proposed [179], where a micron-sized particle performs revolutions around the optical beam when optically trapped in a water-2.6-lutidine critical mixture. The work performed by this engine is adjustable by the power of optical trap, the temperature of the environment and the criticality of the mixture Fig. 6 [179].

4.5. Optical binding

Optical binding describes the spontaneous organisation of large numbers of colloidal particles in an optical field that arises as a result of multiple optical scattering [38,203,204]. It was first observed by Burns et al. [205], who demonstrated an optical binding interaction between a pair of particles in a line-shaped focus by showing that there existed discrete values of the particle's separation in the transverse direction where they formed a stable bound pair. This work was followed by the observation of a large number of particles that 'crystallised' in the interference pattern formed in the transverse plane of the intersection of a number of laser beams [206].

The optical binding interaction can be simply understood by considering a pair of dipoles in an optical field [6]. Consider the case of two dipolar particles arranged parallel to the propagation direction of a laser beam. The first dipole scatters radiation, and the scattered field propagates in the forward direction to impinge on the second dipole but with a fixed phase difference with the incident field. The net effect is to modify the magnitude of the scattering force in the forward direction, but as the phase difference between the two fields is constant the force does not change sign, both particles are pushed in the same direction and the first tends to catch up with the second. Now, if we consider the fields impinging on the first particle, these are the incident field and the fields that is backscattered by the second particle. The phase difference between these fields depends on the relative separation of the particles, and hence the force between the particles oscillated with a change of sign with a period of half the optical wavelength. This gives rise to the observed optical binding interaction and the existence of stable inter-particle separations.

Optical binding may be realised experimentally in a number of configurations. The original experiments of Burns et al. [205,206] used shaped optical fields to produce optical binding in the transverse plane. Longitudinal optical binding can be realised with counter-propagating free-space beams, for example, emerging from a pair of optical fibres [207,208], or with counter-propagating evanescent fields [209,210]. The evanescent field may be generated by a weakly focusing a laser beam onto an interface at an angle just greater than the critical angle for total internal reflection. When the radiation pressure from this beam is balanced by a counter-propagating beam a variety of optically bound structures form that depend on the optical fields configuration and the particle size and optical properties [209,211]. In such experiments video tracking of the Brownian motion of the particles in the optically bound structure provides a powerful technique for evaluating the optical forces and structure form and dynamics [212,213].

An alternative method for creating an evanescent field is to use a waveguide with suitably small dimensions. This scheme was first demonstrated using a channel waveguide in a planar surface, the evanescent field of which can trap and propel micropaticles [214,215]. More recently a tapered optical fibre scheme has been demonstrated for unidirectional transport using a single beam [216,217], and stable trapping using counter-propagating beams [218,219]. Tapered optical fibres are fabricated from standard fibre using a 'heat-and-pull' technique [220] to draw the fibre to micron- or sub-micron dimensions, at which scale the majority of optical power is carried in the evanescent field that extend into the region surrounding the fibre [221]. The high degree of control that can be exerted over the tapering process permits selective excitation of higher modes of the fibre and an extra degree of control over the trapping and binding [222,223].

The optical binding phenomenon is not limited to dielectric particles: optical binding of silver [224] and gold [225] has been observed, with a plasmonic enhancement of binding forces. Nor is it limited to spherical particles: binding of rod-shaped particles (carbon nanotube bundles) has also been demonstrated [10]. In this case, similarly to spherical particles, a variety of bound structures is predicted to occur [226,227].

4.6. Optical force positioning, aggregation, and spectroscopy.

As already pointed out, the behaviour of a nanoparticle in the focal spot of a laser beam is controlled by the balance between the gradient force and the radiation pressure. In ordinary trapping measurements, the radiation pressure must be minimized, aiming at confining the nanoparticle in the optical trap. However, several other interesting applications can be developed by exploiting the pushing effect of the radiation pressure. Optical force printing [228–231] is one of these applications. The all-optical patterning of surfaces is allowed by single-beam trapping and subsequent positioning of Au colloids [228]. However, the process can be improved by directly using the strong axial force acting on a plasmonic nanosphere at resonance wavelengths, which pushes it toward the substrate [229–231]. The use of radiation pressure instead of trapping forces to guide the particle toward the substrate avoids the constraint on the size of the plasmonic particle, which to be trapped must be not larger than approximately 200 nm in diameter [77]. Moreover, by using a Spatial Light Modulator a laser beam can be split into several beams creating an optical pattern, for simultaneous and controlled positioning of nanoparticles on substrates [229].

In this context, it has been shown that surface-enhanced Raman scattering [79] (SERS)-active aggregates can be created on glass substrates by optical manipulation of gold nanorods (AuNRs) in a liquid environment [232,233] containing biomolecules. In fact, due to their very large extinction cross-sections, these AuNRs cannot be optically trapped with visible wavelengths [232]. However, they can be pushed towards the sample chamber glass walls where they aggregate and form hot-spots on which the Raman spectrum of diluted biomolecules can be strongly enhanced. This method combines the great advantage of optical force printing with the capability of spectroscopic detection of molecules directly in liquid environment, which is the ideal condition for bio-inspired research. A number of biomolecules have been studied. First measurements focused on Bovine Serum Albumin (BSA) molecule, for which the Raman limit of detection (LOD) in water has been lowered from 10^{-3} M to 5×10^{-8} M [233]. Another protein, hemoglobin, has been detected at concentrations as low as 1 pM [232], well below the SERS LOD of approximately 100 nM. Results on amino-acids such as phenylalanine [232] and enzymes such as lysozime [232] and catalase [233] have been also reported [232]. This molecular detection technique can be also made protein-selective by functionalising the AuNRs with aptamers, which capture a target biomolecule. Proof-of-concept results have been obtained with ochratoxin A [233], a nephrotic mycotoxin which may contaminate food commodities and wine representing potential public health risk. With this methodology, the toxin has been detected in liquid environment at concentrations as low as 1 μM [233].

Optical positioning of AuNRs is particularly interesting because it is a low cost alternative to much more complex litographic techniques. As a further advantage, it allows an easy and fast way to decorate with metallic particles also not flat substrates, such as three dimensional micro- and nanostructures obtained with direct laser writing by two-photon photopolymerization (TPP) [234–242], opening the way to the realization of hybrid metal-polymer devices such as, for example, spectroscopic probes and sensors.

Optical positioning is not limited to plasmonic particles. Optical forces have been used to manipulate nanosheets [21] of hexagonal boron nitride (h-BN), molibdenum disulfide (MoS_2) and tungsten disulfide (WS_2) obtained by liquid phase exfoliation (LPE). Whereas the weakly absorbing h-BN can be optically trapped, allowing the all-optical measurement of the mean flake size directly in liquid environment, the strongly absorbing MoS_2 and WS_2 nanosheets cannot be confined in the optical trap, due to overwhelming contribution of radiation pressure on gradient force. Thanks to the consequent optical pushing effect, these nanosheets can be used, in association with BSA, to pattern a common microscope slide, without any special surface pre-treatment, in relatively short times (minutes) and directly in liquid environment [21]. Possible applications concern the realization of nanosheet-based devices of interest in photonics [243], optoelectronics [244], and energy storage [245], or of van der Waals heterostructures [246] in which nanosheets of different composition can be stacked on top of each other.

4.7. Critical Casimir forces

The miniaturisation of devices and machines down to the microscopic and nanoscopic scale involves also forces in a more challenging way. Forces of the order of nano- and piconewton need to be generated and applied with nanometric precision. This is challenging because of the presence of thermal fluctuations. Thermal fluctuations are often seen as a nuisance making the behaviour of micro-engines less deterministic and less predictable [201]. However, under appropriate conditions, fluctuations can produce tunable and localized *critical Casimir forces* to drive nanomachines.

Critical Casimir forces are due to the confinement between multiple objects of the density fluctuations in a critical solution close to its critical temperature. One of the most important and useful features of these forces is their dependence on temperature and on the surface properties of the involved objects. Critical Casimir forces were originally predicted in 1978 da Fisher and De Gennes [248], and they have been measured directly only recently in 2008 [249], which spurred a widespread interest in studying their properties with experiments [250–252].

Optical tweezers represent, again, an important tool for the measurements and characterisation of critical Casimir forces in nanodevices. Critical fluctuations can be confined by trapped objects, using HOT, giving rise to critical Casimir forces. Increasing the temperature of the solution toward the critical point, it is possible to characterise the temperature dependence of these forces by the displacement of the confining objects. This displacement can be quantified by digital video microscopy [110] or by photonic force microscopy [111]. Both of these techniques match the spatial and time domains of critical Casimir forces but HOT combined with digital video microscopy provides a more flexible investigation tool.

Recently, blinking HOT and digital video microscopy have been employed to investigate the effects of critical Casimir forces on the dynamics of a pair of colloidal particles in the absence of optical potentials and dispersed in the bulk of a water-2.6-lutidine critical mixture [247,252]. From the measurement of the time dependence of their center-to-center distance, it was determined the relative diffusion and drift velocity of the particles, which are in agreement with the results of numerical simulations of Brownian dynamics based on the critical Casimir forces Fig. 8 [247]. The comparison with these simulations allowed to infer the correlation length of the critical fluctuations, and therefore the intensity of the critical Casimir forces and the distance from the critical temperature, forming the basis of a protocol for the fine tuning of the critical Casimir force field. This possibility provided new opportunities for the design and the realisation of self-assembled nano-structures and nanodevices.

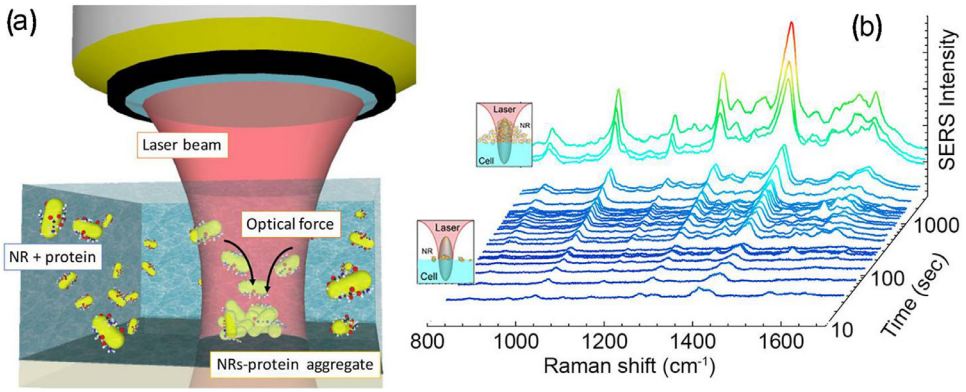

Fig. 7. (a) Sketch of the optical force position and aggregation operation. Nanorods-protein complexes intercepted by a focussed laser beam are optically pushed towards the bottom surface of a glass microfluidic chamber. Here they aggregate, yielding efficient SERS-active clusters. Proteins embedded at the clusters hot spots undergo a strong local field giving rise to a SERS emission that allows to reach picomolar sensitivity in biomolecular detection. (b) SERS emission of BSA-NRs complexes increasing as a function of time during the optical force aggregation process.

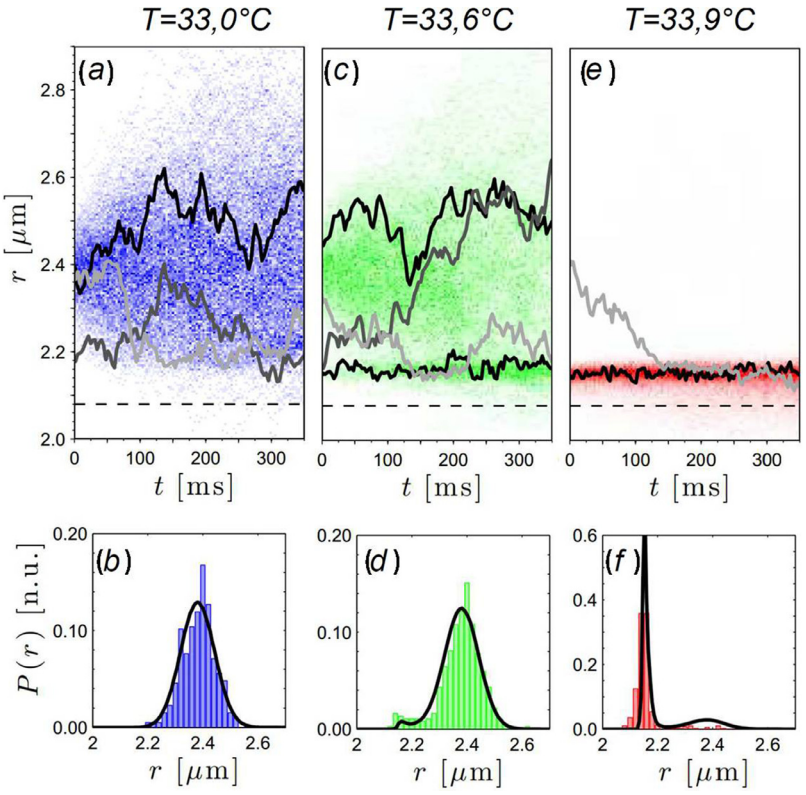

Fig. 8. Effects of critical Casimir forces on the interdistance $r(t)$ of a pair of micro particles, diffusing freely in a water-2.6-lutidine solution at different temperatures. (a, b) At the temperature T=33°C lower than $T_c \approx 34$°C, Critical Casimir forces are not affecting (a) the time distribution r(t) and (b) its spatial distribution P(r) which is Gaussian. (c, d) Increasing the temperature of the solution to T=33, 6°C, critical Casimir forces start to arise affecting (c) $r(t)$ and (d) $P(r)$, which now presents an incipient peak at lower value of r. (e, f) This effect became dominant at the temperature T=33, 9°C, very close to T_c. Here critical Casimir forces prevent the free diffusion of the particles, which are stuck together as showed in panel (e), where all the values of the $r(t)$ are confined within a small region resulting from the equilibrium between attractive critical Casimir forces and repulsive electrostatic forces. (f) At this temperature also the spatial distribution $P(r)$ is strongly affected by critical Casimir forces, presenting a narrow and intense peak corresponding to the equilibrium distance between the particle described before. The solid lines in panels (a,c,e) indicate representative experimental interparticle trajectories while the background colors represents the probability distribution of 400 different $r(t)$, while the dashed horizontal line indicates the interparticle distance corresponding to the diameter of the colloids. Solid lines in panels (b,d,f) are the theoretical distribution of r, obtained via Monte Carlo integration (10^6 samples) of two optically trapped particles subjected to the theoretical total potential [247].

4.8. Stochastic thermodynamics

Optical tweezers can be also employed as a very powerful tool to unveil and characterise the statistical properties of micro- and nanoscopic systems. Here Brownian noise and large thermal fluctuations play a crucial role by introducing stochasticity [254,255]. In particular, the dynamics of optically trapped particles results from the interplay between deterministic optical force fields and Brownian motion, which introduces a well-defined noisy background. Therefore, optically trapped particles can be employed as probes to investigate statistical physics phenomena, whose dynamics are driven by both random and deterministic forces, ranging from biomolecules and nanodevices to financial markets and human organisations.

For the last two decades, optical tweezers have contributed to develop nanothermodynamics, investigating the statical proper-

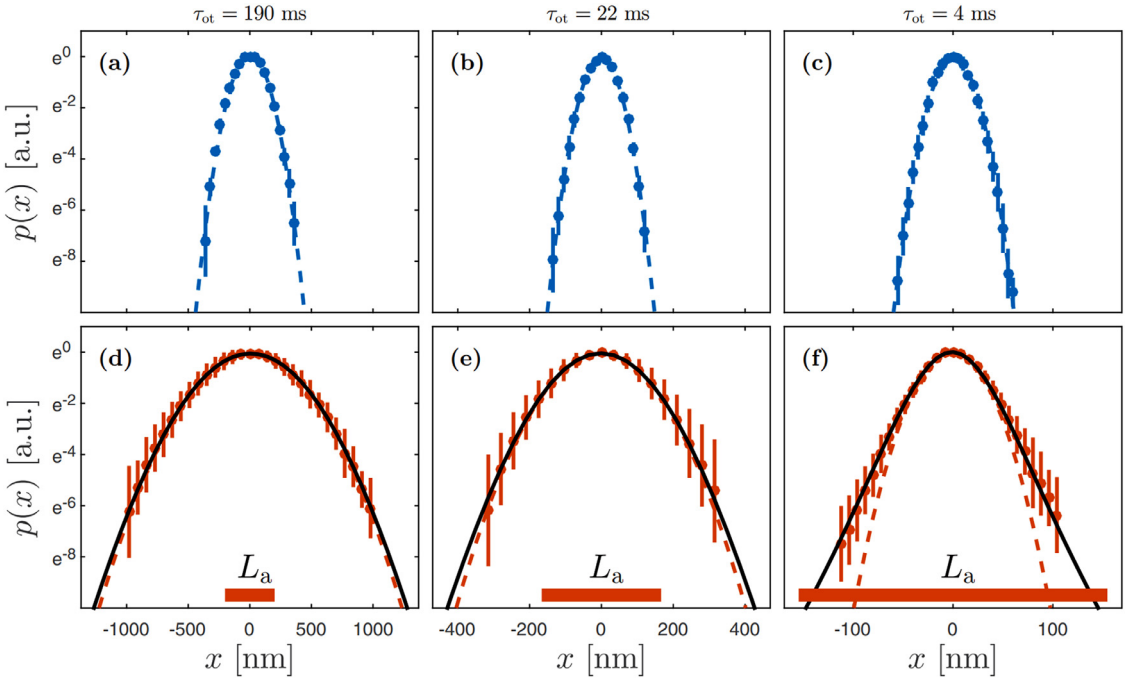

Fig. 9. Emergence of crossover from Boltzman to non-Boltzmann spatial distributions for a trapped particle in an active bath. Dots represent the distribution of an optically trapped particle, while dashed lines correspond to Gaussian distributions. in the case of not active bath, for increasing values of the stiffness (a)=$k = 0.42$ fN nm^{-1}, (b)=$k = 3.6$ fN nm^{-1} and (c)=$k = 22$ fN nm^{-1}, the particle becomes more confined and its spatial distribution remains Gaussian. Vertical lines represent the error on six acquired trajectories. When the particle is trapped in an active bath, as the stiffness increases the particle is confined within a length scale comparable to the persistence length in the active bath (L_a red bar). In this case the particle distribution deviate from Gaussian and can be fitted with a heavy-tailed q-Gaussian distribution (solid black line) with (d) q = 1.013, (e) q = 1.023, and (f) q = 1.142 Panels (d and e). Figure adapted from Argun et al. [253]. (For interpretation of the references to color in this figure legend, the reader is referred to the web version of this article.)

ties of nanosystems to predict the properties and performance of nanoobjects. For example, using trapped colloidal particles, it has been demonstrated that the presence of thermal fluctuations allows the violation of the second law of thermodynamics for small systems over short time scales, even though the second law still holds on average [255].

One of the biggest advances that can be achieved by applying stochastic thermodynamics to microscopic systems is the possibility to recover information about an equilibrium state of the system from measurements where the system is off equilibrium instead of just averaging the fluctuations out [256]. Stochastic thermodynamics can be successfully applied to different systems, such as living matters [257,258]. For example, biomolecules are often coupled, with active baths, due to molecular motors inside the cytoplasm. This coupling is thought to lead to anomalous diffusion within the cytoplasm, a phenomenon that is largely not yet understood [257]. Recently, the behaviour of an optically trapped particle, immersed in an active bath, has been investigated by digital video microscopy to show a transition from Boltzmann to non-Boltzmann statistic [253] (see Fig. 9). This transition takes place whenever the characteristic scale of an optical trap becomes comparable to the characteristic correlation length of the active noise. A consequence of this transition is that non-equilibrium relations such as the Jarzynski equality [259] and Crooks fluctuation theorem [260] cannot be applied in active baths according to their classical formulation [253]. Although this behaviour is unexpected in active system, its investigation is crucial to develop better models for living and far-from-equilibrium systems.

4.9. Active matter

Recently, optical tweezers have proved extremely useful for the characterisation of active matter systems and the study of the interplay between optical forces and thermophoresis. Active matter systems are those systems constituted by natural and artificial objects capable of self-propulsion [261]. Among this category there are systems with different size scales, from bacterial colonies to human crowds. Thanks to their ability in converting energy to propulsion, these systems show behaviours like swarming and the emergence of other collective properties due to far-from equilibrium interactions [262]. This self-propelling behaviour is due to the interplay between random fluctuations (responsible for Brownian motion) and active swimming that drives them into a far-from-equilibrium state. Although self-propulsion is a well-known feature in microorganisms to explore environments for nutrients or to run away from toxic substances [263], a lot of effort is still put in the realization of artificial self-propelling nano and microparticles. Two typical examples of self-propelling particles are artificial Janus particles and biological bacteria such as *Escherichia coli*, both of them well characterised by optical tweezers [264,265]. Furthermore, optical tweezers can be also employed to synchronize collective behaviour of active particles. In particular, this feature has been used to realize a self-assembled fluid pump by trapped active Brownian particles [266]. Optical tweezers can be also employed to perturb the environment of active matter modifying their collective behaviour [267,268]. Recently, it has been proved that the presence of spatial disorder can switch the behaviour of colloidal active matter from aggregative to dispersive [269]. Colloidal particles at equilibrium are always gathered by any attractive potential, but in presence of non-equilibrium driving forces, the particles disperse when spatial disorder is added to the potential. In particular, it has been shown that disordered optical potentials can alter the long-term dynamics of colloidal particles inside an active bacterial bath changing their collective behaviour from aggregative to dispersive [269].

5. Conclusions

Optical tweezers are nowadays a key tool for the contactless manipulation of a wide variety of samples at the micro and nanoscale. The modeling of optical tweezers with accurate T-matrix methods has brought advances in the understanding of experiments on non-spherical particles and the role of shape. Here we discussed some fundamental aspects of the theory and experimental practice of optical tweezers with a focus on a selection of applications in biology, spectroscopy, optical positioning, and nanothermodynamics. After almost 50 years since the pioneering experiments by Arthur Ashkin on optical forces on microparticles, this exciting field is still acquiring momentum expanding its treads to exciting developments from the life sciences [270], to nanoengines [271], and quantum technologies [272].

Acknowledgements

This paper is dedicated to the memory of Ferdinando Borghese, great teacher of light scattering theory, quantum mechanics, and much more.

References

[1] J. Kepler, De cometis. Libelli tres. *Mylius: Augustae Vindelicorum*, 1619. DOI: 10.3931/e-rara-1007.
[2] Ashkin A. Atomic-beam deflection by resonance-radiation pressure. Phys Rev Lett 1970;25(19):1321.
[3] Ashkin A. Acceleration and trapping of particles by radiation pressure. Phys Rev Lett 1970;24(4):156.
[4] Ashkin A. History of optical trapping and manipulation of small-neutral particle, atoms, and molecules. IEEE J Sel Top Quantum Electron 2000;6(6):841–56.
[5] Ashkin A, Dziedzic JM, Bjorkholm JE, Chu S. Observation of a single-beam gradient force optical trap for dielectric particles. Opt Lett 1986;11(5):288–90.
[6] Jones PH, Maragò OM, Volpe G. Optical tweezers: principles and applications. Cambridge, UK: Cambridge University Press; 2015.
[7] Foot CJ. Atomic physics. Oxford University Press; 2005.
[8] Dholakia K, Čižmár T. Shaping the future of manipulation. Nat Photonics 2011;5(6):335–42.
[9] Padgett M, Bowman R. Tweezers with a twist. Nat Photonics 2011;5(6):343–8.
[10] Maragò OM, Jones PH, Gucciardi PG, Volpe G, Ferrari AC. Optical trapping and manipulation of nanostructures. Nat nanotechnol 2013;8(11):807.
[11] Ashkin A, Dziedzic JM, Yamane T. Optical trapping and manipulation of single cells using infrared laser beams. Nature 1987;330(6150):769–71.
[12] Ashkin A, Dziedzic JM. Optical trapping and manipulation of viruses and bacteria. Science 1987;235:1517–21.
[13] Fazal FM, Block SM. Optical tweezers study life under tension. Nat Photonics 2011;5(6):318–21.
[14] Maragò O, Gucciardi P, Jones P. Photonic force microscopy: from femtonewton force sensing to ultra-sensitive spectroscopy. In: Scanning probe microscopy in nanoscience and nanotechnology. Springer; 2010. p. 23–56.
[15] Olof SN, Grieve JA, Phillips DB, Rosenkranz H, Yallop ML, Miles MJ, et al. Measuring nanoscale forces with living probes. Nano Lett 2012;12(11):6018–23.
[16] Chaumet P, Nieto-Vesperinas M. Time-averaged total force on a dipolar sphere in an electromagnetic field. Opt Lett 2000;25(15):1065–7.
[17] Ashkin A. Forces of a single-beam gradient laser trap on a dielectric sphere in the ray optics regime. Biophys J 1992;61(2):569–82.
[18] Borghese F, Denti P, Saija R, Iatì MA. Optical trapping of nonspherical particles in the T-matrix formalism. Opt Express 2007;15(19):11984–98.
[19] Borghese F, Denti P, Saija R, Iatì MA, Maragò OM. Radiation torque and force on optically trapped linear nanostructures. Phys Rev Lett 2008;100(16):163903.
[20] Irrera A, Artoni P, Saija R, Gucciardi PG, Iatì MA, Borghese F, et al. Size-scaling in optical trapping of silicon nanowires. Nano Lett 2011;11(11):4879–84.
[21] Donato MG, Messina E, Foti A, Smart T, Jones P, Iatì MA, et al. Optical trapping and optical force positioning of two-dimensional materials. Nanoscale 2018;10:1245–55. doi:10.1039/C7NR06465A.
[22] Borghese F, Denti P, Saija R. Scattering from model nonspherical particles: theory and applications to environmental physics. Springer Science & Business Media; 2007.
[23] Callegari A, Mijalkov M, Gököz AB, Volpe G. Computational toolbox for optical tweezers in geometrical optics. JOSA B 2015;32(5):B11–19.
[24] Volpe G, Volpe G. Simulation of a Brownian particle in an optical trap. Am J Phys 2013;81(3):224–30.
[25] Ashkin A. Forces of a single-beam gradient laser trap on a dielectric sphere in the ray optics regime. Methods Cell Biol 1997;55:1–27.
[26] Mishchenko M, Travis L, Lacis A. Scattering, absorption, and emission of light by small particles. Cambridge University Press; 2002.
[27] Neto PM, Nussenzveig H. Theory of optical tweezers. EPL (Europhys Lett) 2000;50(5):702.
[28] Mazolli A, Neto PM, Nussenzveig H. Theory of trapping forces in optical tweezers. In: Proceedings of the royal society of london A: mathematical, physical and engineering sciences; vol. 459. The Royal Society; 2003, p. 3021–3041.
[29] Nieminen TA, Stilgoe AB, Heckenberg NR, Rubinsztein-Dunlop H. Approximate and exact modeling of optical trapping. In: Proceedings of the optical trapping and optical micromanipulation VII, 7762. International Society for Optics and Photonics; 2010. p. 77622V.
[30] Gordon JP. Radiation forces and momenta in dielectric media. Phys Rev A 1973;8(1):14.
[31] Arias-González JR, Nieto-Vesperinas M. Optical forces on small particles: attractive and repulsive nature and plasmon-resonance conditions. JOSA A 2003;20(7):1201–9.
[32] Amendola V, Pilot R, Frasconi M, Maragò OM, Iatì MA. Surface plasmon resonance in gold nanoparticles: a review. J Phys Condens Matter 2017;29(20):203002.
[33] Born M, Wolf E. Principles of optics: electromagnetic theory of propagation, interference and diffraction of light. Cambridge, United Kingdom: Cambridge University Press; 1999.
[34] Skelton SE, Sergides M, Memoli G, Maragó OM, Jones PH. Trapping and deformation of microbubbles in a dual-beam fibre-optic trap. J Opt 2012;14(7):075706.
[35] Galajda P, Ormos P. Orientation of flat particles in optical tweezers by linearly polarized light. Opt Express 2003;11(5):446–51.
[36] Galajda P, Ormos P. Complex micromachines produced and driven by light. Appl Phys Lett 2001;78(2):249–51.
[37] Swartzlander GA, Peterson TJ, Artusio-Glimpse AB, Raisanen AD. Stable optical lift. Nat Photonics 2011;5(1):48–51.
[38] Dholakia K, Zemánek P. Colloquium: Gripped by light: optical binding. Rev Modern Phys 2010;82(2):1767.
[39] Draine BT, Goodman J. Beyond Clausius-Mossotti-wave propagation on a polarizable point lattice and the discrete dipole approximation. Astrophys J 1993;405:685–97.
[40] Gao D, Ding W, Nieto-Vesperinas M, Ding X, Rahman M, Zhang T, et al. Optical manipulation from the microscale to the nanoscale: fundamentals, advances and prospects. Light Sci Appl 2017;6(9):e17039.
[41] Albaladejo S, Laroche MIMM, Sáenz JJ. Scattering forces from the curl of the spin angular momentum of a light field. Phys Rev Lett 2009;102(11):113602.
[42] Marqués MI, Sáenz JJ. Reply to comment on scattering forces from the curl of the spin angular momentum of a light field. Phys Rev Lett 2013;111(5):059302.
[43] Zemánek P, Jonáš A, Jákl P, Ježek J, Šerý M, Liška M. Theoretical comparison of optical traps created by standing wave and single beam. Opt Commun 2003;220(4-6):401–12.
[44] Volpe G, Singh GP, Petrov D. Optical tweezers with cylindrical vector beams produced by optical fibers. In: Proceedings of the optical trapping and optical micromanipulation, 5514. International Society for Optics and Photonics; 2004. p. 283–93.
[45] Donato MG, Vasi S, Sayed R, Jones PH, Bonaccorso F, Ferrari AC, et al. Optical trapping of nanotubes with cylindrical vector beams. Opt Lett 2012;37(16):3381–3.
[46] Skelton SE, Sergides M, Saija R, Iatì MA, Maragó OM, Jones PH. Trapping volume control in optical tweezers using cylindrical vector beams. Opt Lett 2013;38(1):28–30.
[47] Marqués MI. Beam conFIGuration proposal to verify that scattering forces come from the orbital part of the poynting vector. Opt Lett 2014;39(17):5122–5.
[48] Berry MV. Optical currents. J Opt A Pure Appl Opt 2009;11(9):094001.
[49] Bliokh KY, Bekshaev AY, Nori F. Extraordinary momentum and spin in evanescent waves. Nat Commun 2014;5:3300.
[50] Antognozzi M, Bermingham CR, Harniman RL, Simpson S, Senior J, Hayward R, et al. Direct measurements of the extraordinary optical momentum and transverse spin-dependent force using a nano-cantilever. Nat Phys 2016;12(8):731.
[51] Triolo C, Cacciola A, Patanè S, Saija R, Savasta S, Nori F. Spin-momentum locking in the near field of metal nanoparticles. ACS Photonics 2017;4(9):2242–9.
[52] Mishchenko MI. Radiation force caused by scattering, absorption, and emission of light by nonspherical particles. J Quant Spectrosc Radiat Transf 2001;70(4-6):811–16.
[53] Nieminen TA, Rubinsztein-Dunlop H, Heckenberg NR. Calculation and optical measurement of laser trapping forces on non-spherical particles. J Quant Spectrosc Radiat Transf 2001;70(4-6):627–37.
[54] Saija R, Iatì MA, Giusto A, Denti P, Borghese F. Transverse components of the radiation force on nonspherical particles in the T-matrix formalism. J Quant Spectrosc Radiat Transf 2005;94(2):163–79.
[55] Pfeifer RN, Nieminen TA, Heckenberg NR, Rubinsztein-Dunlop H. Colloquium: momentum of an electromagnetic wave in dielectric media. Rev Mod Phys 2007;79(4):1197.
[56] Simpson SH. Inhomogeneous and anisotropic particles in optical traps: physical behaviour and applications. J Quant Spectrosc Radiat Transf 2014;146:81–99.
[57] Nieminen TA, Preez-Wilkinson ND, Stilgoe AB, Loke VLY, Bui AAM, Rubinsztein-Dunlop H. Optical tweezers: theory and modelling. J Quant Spectrosc Radiat Transf 2014;146:59–80.

[58] Qi X, Nieminen TA, Stilgoe AB, Loke VL, Rubinsztein-Dunlop H. Comparison of T-matrix calculation methods for scattering by cylinders in optical tweezers. Opt Lett 2014;39(16):4827–30.
[59] Bui AA, Stilgoe AB, Lenton IC, Gibson LJ, Kashchuk AV, Zhang S, et al. Theory and practice of simulation of optical tweezers. J Quant Spectrosc Radiat Transf 2017;195:66–75.
[60] Girard C. Near fields in nanostructures. Rep Prog Phys 2005;68(8):1883.
[61] Yurkin MA, Hoekstra AG. The discrete dipole approximation: an overview and recent developments. J Quant Spectrosc Radiat Transf 2007;106(1-3):558–89.
[62] Yee K. Numerical solution of initial boundary value problems involving Maxwell's equations in isotropic media. IEEE Trans Antennas Propag 1966;14(3):302–7.
[63] Elsherbeni AZ, Demir V. The finite-difference time-domain method for electromagnetics with MATLAB simulations. The Institution of Engineering and Technology; 2016.
[64] Waterman P. Symmetry, unitarity, and geometry in electromagnetic scattering. Phys Rev D 1971;3(4):825.
[65] Gouesbet G, Lock J, Gréhan G. Generalized Lorenz–Mie theories and description of electromagnetic arbitrary shaped beams: localized approximations and localized beam models, a review. J Quant Spectrosc Radiat Transf 2011;112(1):1–27.
[66] Purcell EM, Pennypacker CR. Scattering and absorption of light by nonspherical dielectric grains. Astrophys J 1973;186:705–14.
[67] Draine BT, Flatau PJ. Discrete-dipole approximation for scattering calculations. JOSA A 1994;11(4):1491–9.
[68] Simpson SH, Hanna S. Application of the discrete dipole approximation to optical trapping calculations of inhomogeneous and anisotropic particles. Opt Express 2011;19(17):16526–41.
[69] Simpson SH, Hanna S. Holographic optical trapping of microrods and nanowires. JOSA A 2010;27(6):1255–64.
[70] Phillips D, Padgett M, Hanna S, Ho Y-L, Carberry D, Miles M, et al. Shape-induced force fields in optical trapping. Nat Photonics 2014;8(5):400.
[71] Gauthier RC. Computation of the optical trapping force using an FDTD based technique. Opt Express 2005;13(10):3707–18.
[72] Benito DC, Simpson SH, Hanna S. Fdtd simulations of forces on particles during holographic assembly. Opt Express 2008;16(5):2942–57.
[73] Yang X, Liu Y, Oulton RF, Yin X, Zhang X. Optical forces in hybrid plasmonic waveguides. Nano Lett 2011;11(2):321–8.
[74] Zaman MA, Padhy P, Hesselink L. A semi-analytical model of a near-field optical trapping potential well. J Appl Phys 2017;122(16):163101.
[75] Borghese F, Denti P, Saija R, Toscano G, Sindoni OI. Multiple electromagnetic scattering from a cluster of spheres. I. Theory. Aerosol Sci Technol 1984;3(2):227–35.
[76] Saija R, Iatì MA, Denti P, Borghese F, Giusto A, Sindoni OI. Efficient light-scattering calculations for aggregates of large spheres. Appl Opt 2003;42(15):2785–93.
[77] Saija R, Denti P, Borghese F, Maragó OM, Iatì MA. Optical trapping calculations for metal nanoparticles: comparison with experimental data for Au and Ag spheres.. Opt Express 2009;17:10231–41.
[78] Spadaro D, Iatí M, Pérez-Piñeiro J, Vazquez-Vazquez C, Correa-Duarte M, Donato M, et al. Optical trapping of plasmonic mesocapsules: enhanced optical forces and sers. J Phys Chem C 2016;121(1):691–700.
[79] Amendola V, Pilot R, Frasconi M, Marago OM, Iati MA. Surface plasmon resonance in gold nanoparticles: a review. J Phys Condens Matter 2017;29(20):203002.
[80] Wyatt PJ. Scattering of electromagnetic plane waves from inhomogeneous spherically symmetric objects. Phys Rev 1964;134(7AB):AB1.
[81] Spadaro D, Iatì MA, Donato MG, Gucciardi PG, Saija R, Cherlakola AR, et al. Scaling of optical forces on au–peg core–shell nanoparticles. RSC Adv 2015;5(113):93139–46.
[82] Borghese F, Denti P, Saija R, Sindoni O. Optical properties of spheres containing a spherical eccentric inclusion. JOSA A 1992;9(8):1327–35.
[83] Fucile E, Denti P, Borghese F, Saija R, Sindoni OI. Optical properties of a sphere in the vicinity of a plane surface. J Opt Soc Am A 1997;14(7):1505–14.
[84] Borghese F, Denti P, Saija R, Iatì MA, Sindoni OI. Optical properties of a dispersion of anisotropic particles with non-randomly distributed orientations. The case of atmospheric ice crystals. J Quant Spectrosc Radiat Transf 2001;70(2):237–51.
[85] Mackowski DW, Mishchenko MI. Calculation of the T-matrix and the scattering matrix for ensembles of spheres. JOSA A 1996;13(11):2266–78.
[86] Mie G. Beiträge zur optik trüber medien, speziell kolloidaler metallösungen. Annalen der Physik 1908;330(3):377–445.
[87] Gouesbet G, Gréhan G. Generalized Lorenz–Mie theories. Springer; 2017.
[88] Gouesbet G. T-matrix formulation and generalized Lorenz–Mie theories in spherical coordinates. Opt Commun 2010;283(4):517–21.
[89] Lock JA. Calculation of the radiation trapping force for laser tweezers by use of generalized Lorenz–Mie theory. i. localized model description of an on-axis tightly focused laser beam with spherical aberration. Appl Opt 2004;43(12):2532–44.
[90] Neves AAR, Fontes A, de Y Pozzo L, Thomaz AAD, Chillce E, Rodriguez E, et al. Electromagnetic forces for an arbitrary optical trapping of a spherical dielectric. Opt Express 2006;14(26):13101–6.
[91] Neves AAR, Fontes A, Cesar CL, Camposeo A, Cingolani R, Pisignano D. Axial optical trapping efficiency through a dielectric interface. Phys Rev E 2007;76(6):061917.
[92] Ambrosio LA, Hernández-Figueroa HE. Integral localized approximation description of ordinary bessel beams and application to optical trapping forces. Biomed Opt Express 2011;2(7):1893–906.
[93] Neves AAR. Photonic nanojets in optical tweezers. J Quant Spectrosc Radiat Transf 2015;162:122–32.
[94] Ishimaru A. Wave propagation and scattering in random media and rough surfaces. Proc IEEE 1991;79(10):1359–66.
[95] Borghese F, Denti P, Saija R, Iatì MA. Radiation torque on nonspherical particles in the transition matrix formalism. Opt Express 2006;14(20):9508–21.
[96] Borghese F, Denti P, Saija R, Iati MA. On the rotational stability of nonspherical particles driven by the radiation torque. Opt Express 2007;15(14):8960–71.
[97] Marston PL, Crichton JH. Radiation torque on a sphere caused by a circularly-polarized electromagnetic wave. Phys Rev A 1984;30(5):2508.
[98] Wolf EL. Nanophysics and nanotechnology: an introduction to modern concepts in nanoscience. John Wiley & Sons; 2015.
[99] Alivisatos AP. Semiconductor clusters, nanocrystals and quantum dots. Science 1996;271(5251):933–7.
[100] Gudiksen MS, Lauhon LJ, Wang J, Smith DC, Lieber CM. Growth of nanowire superlattice structures for nanoscale photonics and electronics. Nature 2002;415(6872):617.
[101] Dick KA. A review of nanowire growth promoted by alloys and non-alloying elements with emphasis on Au-assisted III–V nanowires. Prog Cryst Growth Charact Mater 2008;54(3-4):138–73.
[102] Rohrbach A. Stiffness of optical traps: quantitative agreement between experiment and electromagnetic theory. Phys Rev Lett 2005;95(16):168102.
[103] Sultanova N, Kasarova S, Nikolov I. Characteristics of optical polymers in the design of polymer and hybrid optical systems. Bulg J Phys 2013;40(3):258–64.
[104] Marago OM, Jones PH, Bonaccorso F, Scardaci V, Gucciardi PG, Rozhin AG, et al. Femtonewton force sensing with optically trapped nanotubes. Nano Lett 2008;8(10):3211–16.
[105] Pesce G, Volpe G, Maragò OM, Jones PH, Gigan S, Sasso A, et al. Step-by-step guide to the realization of advanced optical tweezers. J Opt Soc Am B 2015;32(5):B84–98.
[106] Briggs A, Kolosov O. Acoustic microscopy, 67. Oxford University Press; 2010.
[107] Irrera A, Magazzú A, Artoni P, Simpson SH, Hanna S, Jones PH, et al. Photonic torque microscopy of the nonconservative force field for optically trapped silicon nanowires. Nano Lett 2016;16(7):4181–8.
[108] Curtis JE, Koss BA, Grier DG. Dynamic holographic optical tweezers. Opt Commun 2002;207(1-6):169–75.
[109] Otto O, Czerwinski F, Gornall JL, Stober G, Oddershede LB, Seidel R, et al. Real-time particle tracking at 10,000 fps using optical fiber illumination. Opt Express 2010;18(22):22722–33.
[110] Crocker JC, Grier DG. Methods of digital video microscopy for colloidal studies. J Colloid Interface Sci 1996;179(1):298–310.
[111] Florin E-L, Pralle A, Stelzer E, Hörber J. Photonic force microscope calibration by thermal noise analysis. Appl Phys A Mater Sci Process 1998;66:S75–8.
[112] Maragó OM, Bonaccorso F, Saija R, Privitera G, Gucciardi PG, Iati MA, et al. Brownian motion of graphene. ACS Nano 2010;4(12):7515–23.
[113] Simpson SH, Hanna S. First-order nonconservative motion of optically trapped nonspherical particles. Phys Rev E 2010;82:031141.
[114] Toe WJ, Ortega-Piwonka I, Angstmann CN, Gao Q, Tan HH, Jagadish C, et al. Nonconservative dynamics of optically trapped high-aspect-ratio nanowires. Phys Rev E 2016;93(2):022137.
[115] Mihiretie B, Snabre P, Loudet J-C, Pouligny B. Optically driven oscillations of ellipsoidal particles. part i: experimental observations. Eur Phys J E 2014;37(12):124.
[116] Cheng Z, Mason TG, Chaikin P. Periodic oscillation of a colloidal disk near a wall in an optical trap. Phys Rev E 2003;68(5):051404.
[117] Magazzú A, Spadaro D, Donato M, Sayed R, Messina E, D'Andrea C, et al. Optical tweezers: a non-destructive tool for soft and biomaterial investigations. Rendiconti Lincei 2015;26(2):203–18.
[118] Buosciolo A, Pesce G, Sasso A. New calibration method for position detector for simultaneous measurements of force constants and local viscosity in optical tweezers. Opt Commun 2004;230(4):357–68.
[119] Coffey W, Kalmykov YP, Waldron JT. The Langevin equation: with applications to stochastic problems in physics, chemistry, and electrical engineering, 14. World Scientific; 2004.
[120] Le Bellac M, Mortessagne F, Batrouni GG. Equilibrium and non-equilibrium statistical thermodynamics. Cambridge University Press; 2004.
[121] Bar-Ziv R, Meller A, Tlusty T, Moses E, Stavans J, Safran SA. Localized dynamic light scattering: probing single particle dynamics at the nanoscale. Phys Rev Lett 1997;78(1):154.
[122] Henderson S, Mitchell S, Bartlett P. Position correlation microscopy: probing single particle dynamics in colloidal suspensions. Coll Surfaces A Physicochem Eng Asp 2001;190(1):81–8.
[123] Mehta AD, Rief M, Spudich JA, Smith DA, Simmons RM. Single molecule biomechanics with optical methods. Science 1999;283:1689–95.
[124] Perkins TT. Optical traps for single molecule biophysics: a primer. Laser Photonics Rev 2009;3:203–20.
[125] Svoboda K, Block SM. Biological applications of optical forces. Annu Rev Biophys Biomol Struct 1994;23:247–85.
[126] Ou-Yang HD, Wei MT. Complex fluids: probing mechanical properties of biological systems with optical tweezers. Ann Rev Phys Chem 2010;61:421–40.
[127] Hénon S, Lenormand G, Richert A, Gallet F. A new determination of the shear modulus of the human erythrocyte membrane using optical tweezers. Biophys J 1999;76(2):1145–51.

[128] Dao M, Lim CT, Suresh S. Mechanics of the human red blood cell deformed by optical tweezers. J Mech Phys Solids 2003;51:2259–80.
[129] Bronkhorst PJ, Streekstra GJ, Grimbergen J, Nijhof EJ, Sixma JJ, Brakenhoff GJ. A new method to study shape recovery of red blood cells using multiple optical trapping. Biophys J 1995;69(5):1666–73.
[130] Liao G-B, Bareil PB, Sheng Y, Chiou A. One-dimensional jumping optical tweezers for optical stretching of bi-concave human red blood cells. Opt Express 2008;16(3):1996–2004.
[131] Rancourt-Grenier S, Wei M-T, Bai J-J, Chiou A, Bareil PP, Duval P-L, et al. Dynamic deformation of red blood cell in dual-trap optical tweezers. Opt Express 2010;18(10):10462–72.
[132] Yu L, Sheng Y, Chiou A. Three-dimensional light-scattering and deformation of individual biconcave human blood cells in optical tweezers. Opt Express 2013;21(10):12174–84.
[133] Yoon Y, Kotar J, Yoon G, Cicuta P. The nonlinear mechanical response of the red blood cell. Phys Biol 2008;5(3):036007.
[134] Yoon YZ, Kotar J, Brown AT, Cicuta P. Red blood cell dynamics: from spontaneous fluctuations to non-linear response. Soft Matter 2011;7:2042–51.
[135] Yu L, Sheng Y. Effect of the object 3d shape on the viscoelastic testing in optical tweezers. Opt Express 2015;23(5):6020–8.
[136] Raj S, Marro M, Wojdyla M, Petrov D. Mechanochemistry of single red blood cells monitored using raman tweezers. Biomed Opt Express 2012;3(4):753–63.
[137] Guck J, Ananthakrishnan R, Mahmood H, Moon TJ, Cunningham CC, Käs J. The optical stretcher: a novel laser tool to micromanipulate cells. Biophys J 2001;81(2):767–84.
[138] Bareil PB, Sheng Y, Chen Y-Q, Chiou A. Calculation of spherical red blood cell deformation in a dual-beam optical stretcher. Opt Express 2007;15(24):16029–34.
[139] Ekpenyong AE, Posey CL, Chaput JL, Burkart AK, Marquardt MM, Smith TJ, et al. Determination of cell elasticity through hybrid ray optics and continuum mechanics modeling of cell deformation in the optical stretcher. Appl Opt 2009;48(32):6344–54.
[140] Mauritz JMA, Esposito A, Tiffert T, Skepper JN, Warley A, Yoon Y-Z, et al. Biophotonic techniques for the study of malaria-infected red blood cells. Med Biol Eng Comput 2010;48(10):1055–63.
[141] Lee S, Joo B, Jeon PJ, Im S, Oh K. Columnar deformation of human red blood cell by highly localized fiber optic bessel beam stretcher. Biomed Opt Express 2015;6(11):4417–32.
[142] Suresh S. Mechanical response of human red blood cells in health and disease: Some structure-property-function relationships. J Mater Res 2006;21(8):1871–7.
[143] Agrawal R, Sherwood J, Chhablani J, Riccharіya A, Kim S, Jones PH, et al. Red blood cells in retinal vascular disorders. Blood Cells, Mol Dis 2016;56(1):53–61.
[144] Suresh S, Spatz J, Mills J, Micoulet A, Dao M, Lim C, et al. Single-cell biomechanics and human disease states: Gastrointestinal cancer and malaria. Acta Biomater 2005;1:16.
[145] Mauritz JM, Tiffert T, Seear R, Lautenschläger F, Esposito A, Lew VL, et al. Detection of plasmodium falciparum-infected red blood cells by optical stretching. J Biomed Opt 2010;15(3):030517.
[146] Agrawal R, Smart TJ, Nobre-Cardoso J, Richards CJ, Bhatnagar R, Tufail A, et al. Assessment of red blood cell deformability in type 2 diabetes mellitus and diabetic retinopathy by dual optical tweezers stretching technique. Sci Rep 2016;6:15873.
[147] Agrawal R, Ang B, Balne PK, Richards C, Smart TJ, Cardoso J, Shima D, Jones PH, Pavesio C. Non-occlusive retinal vascular inflammation and role of red blood cell deformability in birdshot chorioretinopathy. Ocul Immunol Inflamm 2018:1–9. doi:10.1080/09273948.2018.1485959.
[148] Sheikh-Hasani V, Babaei M, Azadbakht A, Pazoki-Toroudi H, Mashaghi A, Moosavi-Movahedi AA, et al. Atorvastatin treatment softens human red blood cells: an optical tweezers study. Biomed Opt Express 2018;9(3):1256–61.
[149] Prentice PA, MacDonald MP, Frank TG, Cuschieri A, Spalding GC, Sibbett W, et al. Manipulation and filtration of low index particles with holographic Laguerre–Gaussian optical trap arrays. Opt Express 2004;12(4):593–600.
[150] Arlt J, Padgett M. Generation of a beam with a dark focus surrounded by regions of higher intensity: the optical bottle beam. Opt Lett 2000;25(4):191–3.
[151] Jones PH, Stride E, Saffari N. Trapping and manipulation of microscopic bubbles with a scanning optical tweezer. Appl Phys Lett 2006;89(8):081113.
[152] Jones PH, Maragó OM, Stride EPJ. Parametrization of trapping forces on microbubbles in scanning optical tweezers. J Opt A Pure Appl Opt 2007;9(8):S278.
[153] Sung S-Y, Lee Y-G. Trapping of a micro-bubble by non-paraxial Gaussian beam: computation using the FDTD method. Opt Express 2008;16(5):3463–73.
[154] Smart TJ, Unlu MB, Jones PH. Microbubble trapping in inverted optical tweezers. Proc SPIE, 10347; 2017. p. 1034731. doi:101117/122274033.
[155] Fury C, Harfield C, Jones PH, Stride E, Memoli G. Experimental characterisation of holographic optical traps for microbubbles. Proc SPIE, 9126; 2014. p. 91263L. doi:101117/122055889.
[156] Fury C, Jones PH, Memoli G. Multiscale manipulation of microbubbles employing simultaneous optical and acoustical trapping. Proc. SPIE, 9164; 2014. 91642Z. doi:10.1117/12.2061622.
[157] Memoli G, Fury CR, Baxter KO, Gélat PN, Jones PH. Acoustic force measurements on polymer-coated microbubbles in a microfluidic device. J Acoust Soc Am 2017;141(5):3364–78.
[158] Harfield CJ, Fury CR, Memoli G, Jones PH, Ovenden N, Stride EPJ. Analysis of the uncertainty in microbubble characterisation. Ultrasound Med Biol 2016;42:1412–18.
[159] Lankers M, Popp J, Rossling G, Kiefer W. Raman investigations on laser–trapped gas bubbles. Chem Phys Lett 1997;277(4):331–4.
[160] Saglimbeni F, Bianchi S, Bolognesi G, Paradossi G, Di Leonardo R. Optical characterization of an individual polymer-shelled microbubble structure via digital holography. Soft Matter 2012;8:8822–5.
[161] Prentice P, Cuschieri A, Dholakia K, Prausnitz M, Campbell P. Membrane disruption by optically controlled microbubble cavitation. Nat Phys 2005;1:107–10.
[162] Beth RA. Mechanical detection and measurement of the angular momentum of light. Phys Rev 1936;50(2):115.
[163] Canaguier-Durand A, Hutchison JA, Genet C, Ebbesen TW. Mechanical separation of chiral dipoles by chiral light. New J Phys 2013;15(12):123037.
[164] Hayat A, Mueller JB, Capasso F. Lateral chirality-sorting optical forces. Proc Nat Acad Sci 2015;112(43):13190–4.
[165] Rukhlenko ID, Tepliakov NV, Baimuratov AS, Andronaki SA, Gunko YK, Baranov AV, et al. Completely chiral optical force for enantioseparation. Sci Rep 2016;6:36884.
[166] Friese MEJ, Nieminen TA, Heckenberg NR, Rubinsztein-Dunlop H. Optical alignment and spinning of laser-trapped microscopic particles. Nature 1998;394:348–50.
[167] Bishop AI, Nieminen TA, Heckenberg NR, Rubinsztein-Dunlop H. Optical microrheology using rotating laser-trapped particles. Phys Rev Lett 2004;92(19):198104.
[168] Bennett JS, Gibson LJ, Kelly RM, Brousse E, Baudisch B, Preece D, et al. Spatially-resolved rotational microrheology with an optically-trapped sphere. Sci Rep 2013;3:1759.
[169] Arita Y, Mazilu M, Dholakia K. Laser-induced rotation and cooling of a trapped microgyroscope in vacuum. Nat Commun 2013;4:2374.
[170] Tkachenko G, Brasselet E. Spin controlled optical radiation pressure. Phys Rev Lett 2013;111:033605.
[171] Tkachenko G, Brasselet E. Optofluidic sorting of material chirality by chiral light. Nat Commun 2014;5:3577.
[172] Tkachenko G, Brasselet E. Helicity-dependent three-dimensional optical trapping of chiral microparticles. Nat Commun 2014;5:4491.
[173] Hernández RJ, Mazzulla A, Pane A, Volke-Sepúlveda K, Cipparrone G. Attractive-repulsive dynamics on light-responsive chiral microparticles induced by polarized tweezers. Lab Chip 2013;13:459–67.
[174] Hernández R, Mazzulla A, Provenzano C, Pagliusi P, Cipparrone G. Chiral resolution of spin angular momentum in linearly polarized and unpolarized light. Sci Rep 2015;5:16926.
[175] Cipparrone G, Mazzulla A, Pane A, Hernandez RJ, Bartolino R. Chiral self-assembled solid microspheres: a novel multifunctional microphotonic device. Adv Mater 2011;23:5773–8.
[176] Donato MG, Hernandez J, Mazzulla A, Provenzano C, Saija R, Sayed R, et al. Polarization-dependent optomechanics mediated by chiral microresonators. Nat Commun 2014;5:3656.
[177] Donato M, Mazzulla A, Pagliusi P, Magazzù A, Hernandez R, Provenzano C, et al. Light-induced rotations of chiral birefringent microparticles in optical tweezers. Sci Rep 2016;6:31977.
[178] Seč D, Porenta T, Ravnik M, Žumer S. Geometrical frustration of chiral ordering in cholesteric droplets. Soft Matter 2012;8(48):11982–8.
[179] Schmidt F, Magazzù A, Callegari A, Biancofiore L, Cichos F, Volpe G. Microscopic engine powered by critical demixing. Phys Rev Lett 2018;120(6):068004.
[180] Abdelmohsen LK, Peng F, Tu Y, Wilson DA. Micro-and nano-motors for biomedical applications. J Mater Chem B 2014;2(17):2395–408.
[181] Browne WR, Feringa BL. Making molecular machines work. Nat Nanotechnol 2006;1(1):25.
[182] Sinclair G, Jordan P, Courtial J, Padgett M, Cooper J, Laczik ZJ. Assembly of 3-dimensional structures using programmable holographic optical tweezers. Opt Exp 2004;12(22):5475–80.
[183] Grier DG. A revolution in optical manipulation. Nature 2003;424(6950):810.
[184] Jones P, Palmisano F, Bonaccorso F, Gucciardi P, Calogero G, Ferrari A, et al. Rotation detection in light-driven nanorotors. ACS Nano 2009;3(10):3077–84.
[185] Neves AAR, Camposeo A, Pagliara S, Saija R, Borghese F, Denti P, et al. Rotational dynamics of optically trapped nanofibers. Opt Express 2010;18(2):822–30.
[186] Lehmuskero A, Ogier R, Gschneidtner T, Johansson P, Kall M. Ultrafast spinning of gold nanoparticles in water using circularly polarized light. Nano Lett 2013;13(7):3129–34.
[187] Lehmuskero A, Johansson P, Rubinsztein-Dunlop H, Tong L, Kall M. Laser trapping of colloidal metal nanoparticles. ACS Nano 2015;9(4):3453–69.
[188] Marago O, Gucciardi P, Bonaccorso F, Calogero G, Scardaci V, Rozhin A, et al. Optical trapping of carbon nanotubes. Phys E Low Dimens Syst Nanostructures 2008;40(7):2347–51.
[189] Hansen PM, Bhatia VK, Harrit N, Oddershede L. Expanding the optical trapping range of gold nanoparticles. Nano Lett 2005;5(10):1937–42.
[190] Messina E, Cavallaro E, Cacciola A, Iatì MA, Gucciardi PG, Borghese F, et al. Plasmon-enhanced optical trapping of gold nanoaggregates with selected optical properties. ACS Nano 2011;5(2):905–13.
[191] Messina E, Cavallaro E, Cacciola A, Saija R, Borghese F, Denti P, et al. Manipulation and raman spectroscopy with optically trapped metal nanopar-

ticles obtained by pulsed laser ablation in liquids. J Phys Chem C 2011;115(12):5115–22.
[192] Messina E, D'Urso L, Fazio E, Satriano C, Donato M, D'Andrea C, et al. Tuning the structural and optical properties of gold/silver nano-alloys prepared by laser ablation in liquids for optical limiting, ultra-sensitive spectroscopy, and optical trapping. J Quant Spectrosc Radiat Transf 2012;113(18):2490–8.
[193] Brzobohatỳ O, Šiler M, Trojek J, Chvátal L, Karásek V, Paták A, et al. Three-dimensional optical trapping of a plasmonic nanoparticle using low numerical aperture optical tweezers. Sci Rep 2015;5:8106.
[194] Brzobohaty O, Šiler M, Trojek J, Chvátal L, Karásek V, Zemánek P. Non-spherical gold nanoparticles trapped in optical tweezers: shape matters. Opt Express 2015;23(7):8179–89.
[195] Padgett M, Di Leonardo R. Holographic optical tweezers and their relevance to lab on chip devices. Lab Chip 2011;11(7):1196–205.
[196] Simpson N, Dholakia K, Allen L, Padgett M. Mechanical equivalence of spin and orbital angular momentum of light: an optical spanner. Opt Lett 1997;22(1):52–4.
[197] Ladavac K, Grier DG. Microoptomechanical pumps assembled and driven by holographic optical vortex arrays. Opt Express 2004;12(6):1144–9.
[198] Kao J, Wang X, Warren J, Xu J, Attinger D. A bubble-powered micro-rotor: conception, manufacturing, assembly and characterization. Journal of Micromechanics and Microengineering 2007;17(12):2454.
[199] Lee C, Liamini M, Frechette LG. A silicon microturbopump for a rankine-cycle power-generation microsystem - part ii: Fabrication and characterization. J Microelectromechanical Syst 2011;20(1):326–38.
[200] Quinto-Su PA. A microscopic steam engine implemented in an optical tweezer. Nat Commun 2014;5:5889.
[201] Blickle V, Bechinger C. Realization of a micrometre-sized stochastic heat engine. Nat Phys 2012;8(2):143.
[202] Martínez IA, Roldán É, Dinis L, Petrov D, Parrondo JM, Rica RA. Brownian carnot engine. Nat Phys 2016;12(1):67.
[203] Čižmár T, Dávila Romera LC, Dholakia K, Andrews DL. Multiple optical trapping and binding: new routes to self-assembly. J Phys B At Mol Opt Phys 2010;43:102001.
[204] Bowman RW, Padgett MJ. Optical trapping and binding. Rep Prog Phys 2013;76:026401.
[205] Burns MM, Fournier J-M, Golovchenko JA. Optical binding. Phys Rev Lett 1989;63:1233–6.
[206] Burns MM, Fournier J-M, Golovchenko JA. Optical matter: crystallization and binding in intense optical fields. Science 1990;249(4970):749–54.
[207] Singer W, Frick M, Bernet S, Ritsch-Marte M. Self-organized array of regularly spaced microbeads in a fiber-optical trap. J Opt Soc Am B 2003;20(7):1568–74.
[208] Gordon R, Kawano M, Blakely JT, Sinton D. Optohydrodynamic theory of particles in a dual-beam optical trap. Phys Rev B 2008;77:245125.
[209] Garcés-Chávez V, Dholakia K, Spalding GC. Extended-area optically induced organization of microparticles on a surface. Appl Phys Lett 2005;86(3):031106.
[210] Mellor CD, Bain CD. Array formation in evanescent waves. ChemPhysChem 2006;7(2):329–32.
[211] Mellor CD, Fennerty TA, Bain CD. Polarization effects in optically bound particles arrays. Opt Express 2006;14(21):10079–88.
[212] Han X, Jones PH. Evanescent wave optical binding forces on spherical microparticles. Opt Lett 2015;40(17):4042–5.
[213] Han X, Luo H, Xiao G, Jones PH. Optically bound colloidal lattices in evanescent optical fields. Opt Lett 2016;41(21):4935–8.
[214] Kawata S, Tani T. Optically driven mie particles in an evanescent field along achanneled waveguide. Opt Lett 1996;21(21):1768–70.
[215] Tanaka T, Yamamoto S. Optically induced propulsion of small particles in an evenescent field of higher propagation mode in a multimode, channeled waveguide. Appl Phys Lett 2000;77(20):3131–3.
[216] Brambilla G, Murugan GS, Wilkinson JS, Richardson DJ. Optical manipulation of microspheres along a subwavelength optical wire. Opt Lett 2007;32(20):3041–3.
[217] Skelton SE, Sergides M, Patel R, Karczewska E, Maragó OM, Jones PH. Evanescent wave optical trapping and transport of micro-and nanoparticles on tapered optical fibers. J Quant Spectrosc Radiat Transf 2012;113(18):2512–20.
[218] Sergides M, Skelton SE, Karczewska E, Thorneycroft K, Maragò OM, Jones PH. Optically bound particle structures in evanescent wave traps. Proc. SPIE, 8458; 2012. 84583C. doi:10.1117/12.929612.
[219] Daly M, Truong VG, Chormaic SN. Evanescent field trapping of nanoparticles using nanostructured ultrathin optical fibers. Opt Express 2016;24(13):14470–82.
[220] Ward JM, Maimaiti A, Le VH, Chormaic SN. Contributed review: optical micro- and nanofiber pulling rig. Rev Sci Instrum 2014;85(11):111501.
[221] Daly M, Marios MS, Chormaic SN. Optical trapping and manipulation of micrometer and submicrometer particles. Laser Photonics Rev 2015;9(3):309–29.
[222] Frawley MC, Gusachenko I, Truong VG, Sergides M, Chormaic SN. Selective particle trapping and optical binding in the evanescent field of an optical nanofiber. Opt Express 2014;22(13):16322–34.
[223] Maimaiti A, Truong VG, Sergides M, Gusachenko I, Chormaic SN. Higher order microfibre modes for dielectric particle trapping and propulsion. Sci Rep 2015;5:9077. doi:10.1038/srep09077.
[224] Yan Z, Shah RA, Chado G, Gray SK, Pelton M, Scherer NF. Guiding spatial arrangements of silver nanoparticles by optical binding interactions in shaped light fields. ACS Nano 2013;7(2):1790–802.
[225] Demergis V, Florin E. Ultrastrong optical binding of metallic nanoparticles. Nano Lett 2012;12(11):5756–60.
[226] Simpson SH, Jones PH, Maragò OM, Hanna S, Miles MJ. Optical binding of nanowires in counterpropagating beams. Proc SPIE, 8810; 2013. p. 881026. doi:101117/122024466. 8810–8810–9
[227] Simpson SH, Zemánek P, Maragò OM, Jones PH, Hanna S. Optical binding of nanowires. Nano Lett 2017;17(6):3485–92.
[228] Guffey MJ, Scherer NF. All-optical patterning of Au nanoparticles on surfaces using optical traps. Nano Lett 2010;10(11):4302–8.
[229] Nedev S, Urban AS, Lutich AA, Feldmann J. Optical force stamping lithography. Nano Lett 2011;11(11):5066–70.
[230] Urban AS, Pfeiffer T, Fedoruk M, Lutich AA, Feldmann J. Single-step injection of gold nanoparticles through phospholipid membranes. ACS Nano 2011;5(5):3585–90.
[231] Gargiulo J, Violi IL, Cerrota S, Chvatal L, Cortes E, Perassi EM, et al. Accuracy and mechanistic details of optical printing of single Au and Ag nanoparticles. ACS Nano 2017;11(10):9678–88.
[232] Fazio B, D'Andrea C, Foti A, Messina E, Irrera A, Donato MG, et al. Sers detection of biomolecules at physiological ph via aggregation of gold nanorods mediated by optical forces and plasmonic heating. Sci Rep 2016;6:26952.
[233] Foti A, D'Andrea C, Villari V, Micali N, Donato MG, Fazio B, et al. Optical aggregation of gold nanoparticles for sers detection of proteins and toxins in liquid environment: towards ultrasensitive and selective detection. Materials 2018;11:440.
[234] Sun H-B, Kawata S. Two-photon photopolymerization and 3d lithographic microfabrication. Adv Polym Sci 2004;170:169–274.
[235] Liberale C, Cojoc G, Candeloro P, Das G, Gentile F, De Angelis F, et al. Micro-optics fabrication on top of optical fibers using two-photon lithography. IEEE Photonics Technol Lett 2010;22(7):474–6.
[236] Liberale C, Cojoc G, Bragheri F, Minzioni P, Perozziello G, La Rocca R, et al. Integrated microfluidic device for single-cell trapping and spectroscopy. Sci Rep 2013;3:1258.
[237] Nelson G, Kirian RA, Weierstall U, Zatsepin NA, Faragó T, Baumbach T, et al. Three-dimensional-printed gas dynamic virtual nozzles for x-ray laser sample delivery. Opt Express 2016;24(11):11515–30.
[238] Hengsbach S, Lantada AD. Rapid prototyping of multi-scale biomedical microdevices by combining additive manufacturing technologies. Biomed Microdevices 2014;16(4):617–27.
[239] Dorin B, Parkinson P, Scully P. Direct laser write process for 3d conductive carbon circuits in polyimide. J Mater Chem C 2017;5(20):4923–30.
[240] Klein F, Richter B, Striebel T, Franz CM, Freymann Gv, Wegener M, et al. Two–component polymer scaffolds for controlled three-dimensional cell culture. Adv Mater 2011;23(11):1341–5.
[241] Richter B, Hahn V, Bertels S, Claus TK, Wegener M, Delaittre G, et al. Guiding cell attachment in 3d microscaffolds selectively functionalized with two distinct adhesion proteins. Adv Mater 2017;29(5):1604342.
[242] De Angelis F, Liberale C, Coluccio M, Cojoc G, Di Fabrizio E. Emerging fabrication techniques for 3d nano-structuring in plasmonics and single molecule studies. Nanoscale 2011;3(7):2689–96.
[243] Britnell L, Ribeiro R, Eckmann A, Jalil R, Belle B, Mishchenko A, et al. Strong light-matter interactions in heterostructures of atomically thin films. Science 2013;340(6138):1311–14.
[244] Wang QH, Kalantar-Zadeh K, Kis A, Coleman JN, Strano MS. Electronics and optoelectronics of two-dimensional transition metal dichalcogenides. Nat Nanotechnol 2012;7(11):699–712.
[245] Bonaccorso F, Colombo L, Yu G, Stoller M, Tozzini V, Ferrari AC, et al. Graphene, related two-dimensional crystals, and hybrid systems for energy conversion and storage. Science 2015;347(6217):1246501.
[246] Geim AK, Grigorieva IV. Van der waals heterostructures. Nature 2013;499(7459):419–25.
[247] Magazzù A., callegari A., Staforelli J.P., Gambassi A., Dietrich S., Volpe G. Controlling the dynamics of colloidal particles by critical casimir forces. 2018. arXiv:180611403.
[248] Fisher ME, de Gennes PG. Phénomèenes aux parois dans un mélange binaire critique. C R Acad Sci Paris 1978;B 287:207–9.
[249] Hertlein C, Helden L, Gambassi A, Dietrich S, Bechinger C. Direct measurement of critical Casimir forces. Nature 2008;451(7175):172.
[250] Gambassi A, Maciołek A, Hertlein C, Nellen U, Helden L, Bechinger C, et al. Critical Casimir effect in classical binary liquid mixtures. Phys Rev E 2009;80(6):061143.
[251] Marino E, Kodger TE, ten Hove JB, Velders AH, Schall P. Assembling quantum dots via critical Casimir forces. Sol Energy Mater Sol Cells 2016;158:154–9.
[252] Paladugu S, Callegari A, Tuna Y, Barth L, Dietrich S, Gambassi A, et al. Nonadditivity of critical Casimir forces. Nat Commun 2016;7:11403.
[253] Argun A, Moradi A-R, Pinçe E, Bagci GB, Imparato A, Volpe G. Non-Boltzmann stationary distributions and nonequilibrium relations in active baths. Phys Rev E 2016;94(6):062150.
[254] Evans DJ, Cohen EGD, Morriss GP. Probability of second law violations in shearing steady states. Phys Rev Lett 1993;71(15):2401.
[255] Wang G, Sevick EM, Mittag E, Searles DJ, Evans DJ. Experimental demonstration of violations of the second law of thermodynamics for small systems and short time scales. Phys Rev Lett 2002;89(5):050601.
[256] Jarzynski C. Equalities and inequalities: Irreversibility and the second law

of thermodynamics at the nanoscale. Annu Rev Condens Matter Phys 2011;2(1):329–51.
[257] Barkai E, Garini Y, Metzler R. Strange kinetics of single molecules in living cells. Phys Today 2012;65(8):29.
[258] Bechinger C, Di Leonardo R, Löwen H, Reichhardt C, Volpe G, Volpe G. Active particles in complex and crowded environments. Rev Modern Phys 2016;88(4):045006.
[259] Jarzynski C. Nonequilibrium equality for free energy differences. Phys Rev Lett 1997;78(14):2690.
[260] Crooks GE. Entropy production fluctuation theorem and the nonequilibrium work relation for free energy differences. Phys Rev E 1999;60(3):2721.
[261] Ramaswamy S. The mechanics and statistics of active matter. Annu Rev Condens Matter Phys 2010;1:323–45.
[262] Schweitzer F. Brownian agents and active particles: collective dynamics in the natural and social sciences. Springer Science & Business Media; 2007.
[263] Lauga E, Powers TR. The hydrodynamics of swimming microorganisms. Rep Prog Phys 2009;72(9):096601.
[264] Jiang H-R, Yoshinaga N, Sano M. Active motion of a janus particle by self-thermophoresis in a defocused laser beam. Phys Rev Lett 2010;105(26):268302.
[265] Berg HC. E. coli in Motion. Springer Science & Business Media; 2008.
[266] Hennes M, Wolff K, Stark H. Self-induced polar order of active Brownian particles in a harmonic trap. Phys Rev Lett 2014;112(23):238104.
[267] Leoni M, Kotar J, Bassetti B, Cicuta P, Lagomarsino MC. A basic swimmer at low Reynolds number. Soft Matter 2009;5(2):472–6.
[268] Block SM, Blair DF, Berg HC. Compliance of bacterial flagella measured with optical tweezers. Nature 1989;338(6215):514.
[269] Pinçe E, Velu SK, Callegari A, Elahi P, Gigan S, Volpe G, et al. Disorder-mediated crowd control in an active matter system. Nat Commun 2016;7:10907.
[270] Ha T. Probing nature's nanomachines one molecule at a time. Biophys J 2016;110(5):1004.
[271] Martínez IA, Roldán É, Dinis L, Rica RA. Colloidal heat engines: a review. Soft Matter 2017;13(1):22–36.
[272] Gieseler J, Millen J. Levitated nanoparticles for microscopic thermodynamics - a review. Entropy 2018;20(5):326.